Towards quantitative treatment of electron pair distribution function

Tatiana E. Gorelik, Reinhard Neder, Maxwell W. Terban, Zhongbo Lee, Xiaoke Mu, Christoph Jung, Timo Jacob and Ute Kaiser

Towards quantitative treatment of electron pair distribution function

Tatiana E. Gorelik,[a]* Reinhard Neder,[b] Maxwell W. Terban,[c] Zhongbo Lee,[a] Xiaoke Mu,[d] Christoph Jung,[e,f] Timo Jacob[e,f,g] and Ute Kaiser[a]

[a]Central Facility for Electron Microscopy, University of Ulm, Albert Einstein Allee 11, Ulm, 89081, Germany, [b]Department of Condensed Matter Physics, Friedrich-Alexander University Erlangen-Nürnberg, Staudtstr. 3, Erlangen, 91058, Germany, [c]Max Planck Institute for Solid State Research, Heisenbergstr. 1, Stuttgart, 70569, Germany, [d]Institute of Nanotechnology, Karlsruhe Institute of Technology (KIT), Hermann-von-Helmholtz-Platz 1, Eggenstein-Leopoldshafen, 76344, Germany, [e]Helmholtz Institute Ulm (HIU) Electrochemical Energy Storage, Helmholtzstr. 11, Ulm, 89081, Germany, [f]Karlsruhe Institute of Technology (KIT), PO Box 3640, Karlsruhe, 76021, Germany, and [g]Institute of Electrochemistry, Ulm University, Albert-Einstein Allee 47, Ulm, 89081, Germany. *Correspondence e-mail: tatiana.gorelik@uni-ulm.de

The pair distribution function (PDF) is a versatile tool to describe the structure of disordered and amorphous materials. Electron PDF (ePDF) uses the advantage of strong scattering of electrons, thus allowing small volumes to be probed and providing unique information on structure variations at the nanoscale. The spectrum of ePDF applications is rather broad: from ceramic to metallic glasses and mineralogical to organic samples. The quantitative interpretation of ePDF relies on knowledge of how structural and instrumental effects contribute to the experimental data. Here, a broad overview is given on the development of ePDF as a structure analysis method and its applications to diverse materials. Then the physical meaning of the PDF is explained and its use is demonstrated with several examples. Special features of electron scattering regarding the PDF calculations are discussed. A quantitative approach to ePDF data treatment is demonstrated using different refinement software programs for a nanocrystalline anatase sample. Finally, a list of available software packages for ePDF calculation is provided.

1. Introduction

Knowledge of the atomic positions in a solid is a fundamental basis for the understanding and design of its physical properties. A century-long history of single-crystal structure determination has progressed this method into a well established procedure for determining the atomic coordinates within crystals (Shmueli, 2007). Very small crystals, which are not able to produce sufficient scattering signal alone, can be studied as an assembly; crystallographic methods of crystal structure determination from powders have developed into a widely spread and accepted technique (Cerny & Favre-Nicolin, 2007; David & Shankland, 2008). Single crystal structure determination from electron diffraction data has pushed the required crystal size to a lower limit. Numerous examples of structure analysis of nanocrystalline materials from electron diffraction data can be found in the special issue on electron crystallography (Haderman & Palatinus, 2019) published in *Acta Crystallographica Section B*.

Classical crystallographic methods rely on the solid to possess periodicity at least to some extent, with diffraction patterns that show pronounced Bragg peaks. Poorly crystalline or amorphous materials typically do not produce diffraction
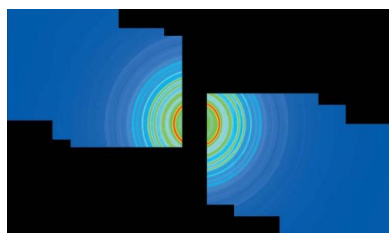
data with sharp and well-resolved Bragg reflections, and therefore cannot be studied using the classical approach. The structure of such materials is assessed using total scattering diffraction data (a continuous scattering curve instead of discrete Bragg reflections), usually measured through X-ray or neutron scattering. The scattering data are usually transformed to direct space giving the pair distribution function (PDF), which is then used for the structure characterization (Egami & Billinge, 2012).

Analysis of PDF data delivers unique information on the local structure of bulk materials (Billinge *et al.*, 1996; Petkov *et al.*, 2000; Billinge, 2008), can aid in understanding the local environment in mesoporous systems (Pauly *et al.*, 1999; Billinge *et al.*, 2005; Chapman *et al.* 2006) and is a vital tool for the characterization of nanoparticles such as the determination of size, defect density and internal strain in the particle (Page *et al.*, 2004; Gilbert *et al.*, 2004, 2013; Michel *et al.*, 2007; Pradhan *et al.*, 2007; Jensen *et al.*, 2012; Manceau *et al.*, 2014).

Diffraction data for PDF calculation is obtained in a powder diffraction experiment. In order to ensure quality of the PDF curve, diffraction data measured to high scattering momentum transfer are needed. Usually scattering data for PDF calculation is measured using short-wavelength X-rays (synchrotron) and neutrons. The most critical experimental demand on the diffraction data for PDF analysis, the large scattering momentum transfer range, can easily be achieved in an electron diffraction experiment through a modification of the electron wavelength, or even easier, through a decrease of the electron diffraction camera length (effective de-magnification of the diffraction pattern when projected onto a detector). Hence, in principle, PDF analysis can be performed using electron diffraction data in the same way as using data from X-ray or neutron diffraction.

Compared to X-rays or neutrons, electrons have the benefit of interacting much more strongly with the sample, resulting in a much stronger scattering signal. As a result, even a tiny sample volume can produce a sufficient signal without the need for specialized equipment, techniques or sample preparation any different than for a usual transmission electron microscopy (TEM) sample (Cockayne, 2007). The PDF methodology can be used for electron scattering just as for X-rays and neutrons.

As a method of structure characterization, ePDF was born in Australia in 1980s. The first materials to be structurally characterized by ePDF were amorphous carbon, silicon and silicon carbide layers prepared by a glow-discharge decomposition of silane/methane mixtures (Sproul *et al.*, 1986). The data was acquired using an energy filtering system. The comparison of PDFs of the samples with different stoichiometry allowed conclusions to be drawn on the phase homogeneity of the sample, so for the samples with high carbon content, the presence of carbon-rich regions was proposed. Comparing the differences in PDFs of a number of tetrahedrally bounded semiconductors, Cockayne & McKenzie (1988) detected bond-angle distortions in amorphous germanium and silicon carbide layers, whereas the carbon tetrahedra in glassy carbon had better defined geometry. The authors connected the stiffness of the carbon tetrahedra with the high hardness of diamond.

The technique was rapidly developing, the obtained PDFs gave accurate nearest-neighbor distances for different atomic species, even in a mixture, yet, there were considerable difficulties in obtaining reliable coordination numbers from the peak intensities. The PDF formalism assumes single elastic electron scattering. The accuracy of this assumption depends on the specimen thickness and the elastic mean free path. If the specimen thickness exceeds the value for the electron mean free path at a given electron wavelength, multiple scattering will occur. Thus, for a given sample thickness, knowledge of the mean free path allows the amount of multiple scattering in the data to be estimated.

The effect of the multiple scattering could be eliminated using either deconvolution techniques (Egerton, 1986; Anstis *et al.*, 1988) or by optimizing the specimen thickness or electron energies such that multiple scattering is negligible. For thin Ni and Ni–Ti alloy foils, the coordination numbers with an uncertainty of below 5% were determined (Hall & Cockayne, 1993).

As reliable PDF data could be obtained for amorphous materials, the structure of these materials could be analyzed. McCulloch *et al.* (1999) were the first to combine ePDF with molecular dynamics simulations to characterize the structure of glassy carbon and amorphous AlN. A few years later, a rather complex amorphous structure of Fe–Zr–B alloy was studied from electron PDF (Hirotsu *et al.*, 2003) supported with the earlier reported reverse Monte Carlo (RMC) simulations (Duine *et al.*, 1994). This was the first work attempting a quantitative fit between the experimental and the simulated data. No note of instrumental contributions to the PDF was made in the paper. The final structural model consisted of deformed body-centered cubic clusters. A similar structural analysis of Ar-irradiation produced amorphous SiC (Hirotsu *et al.*, 2003) showed that along with the Si—C bonds, the material contained homo-atomic C—C and Si—Si bonds; thus the material was non-homogeneous, but contained carbon-rich and silicon-rich areas.

The two factors limiting the quantitative use of electron PDF are *inelastic* and *multiple scattering*. In a similar way to elastic scattering, the probability of inelastic scattering is described with the inelastic cross section and the mean-free path associated with it. The inelastic scattering problem could be successfully resolved by the use of zero-loss energy filtering, either in- or post-column. Different slit widths were used, ranging from 3 eV (Sproul *et al.*, 1986) to 15 eV (Hirotsu *et al.*, 2003). To our knowledge, no systematic study on the effect of the slit width has been published so far. The contribution of multiple scattering was either reduced by thinning the sample or directly extracted from the data by the convolution formalism (Ankele *et al.*, 2005). The extraction of the single scattering contribution improved the fit to the expected PDF, yet required the exact knowledge on the sample thickness and density. Another innovation presented in this publication was the use of shifted diffraction patterns on the detector with subsequent stitching of the data. This technique

not only allowed the free selection of the scattering range, but also a significant reduction of the noise in the data though a variable exposure.

A different strategy for the extraction of the single scattering contribution was presented by Petersen and co-workers (Petersen *et al.*, 2005) based on an acquisition of diffraction data with different wavelengths. The effect of multiple scattering is much more strongly pronounced for lower electron wavelengths, and can thus be efficiently eliminated from the data. The use of the multiple-wavelength formalism was applied to glassy carbon and cross-correlated with the neutron and X-ray scattering data. The so-corrected data showed significantly improved fit to neutron and X-rays.

An elegant study combining electron PDF, nano-electron beam diffraction with the beam diameter of approximately 1 nm and RMC simulations was presented by Hirata and co-workers (Hirata *et al.*, 2006b). The combination of methods was applied to amorphous Fe–B samples with different stoichiometries. Nano-beam diffraction showed local atomic arrangement, which then was interpreted as atomic clusters. The co-existence of different geometries of atomic clusters was assigned to the nanoscale phase separation. These clusters were fed into the RMC model and refined against the electron PDF. The final structure showed that the most prevalent structure element was the B-centered trigonal prism with three capping atoms. A similar strategy applied to Pd–Ni–P metallic glass showed a nanoscale phase separation with intact face-centered domains of a few nanometres surrounded by the disordered material (Hirata *et al.*, 2006a). The analysis of Zr–Ni and Zr–Cu glasses showed that the Zr–Ni sample contained islands of the crystalline Zr_2Ni phase (the primary phase in the crystallization process), while Zr–Cu had a more isotropic arrangement (Hirata *et al.*, 2007).

The discovery of metallic glasses in 1960 (Klement *et al.*, 1960) boosted the interest in non-crystalline materials. Electron diffraction experiments were of particular interest for these systems, as they could spot structural variations within the amorphous matrix. Local rearrangement within the first- and second-order coordination shells was reported for Al–La–Ni glass observed by ePDF and supported by RMC structure simulations (Li *et al.*, 2009). The structural fluctuations were proposed to be the basis for the material's ductility. Local coordination polyhedral models were built for magnetically anisotropic thin CoFeB films based on ePDF data; no structural anisotropy was detected within the sensitivity of the method (Kirk *et al.*, 2009). A mechanism for fast switching between the amorphous and crystalline phases of Ge–Sb–Te through plane rotations, similar to those in Rubik's cube, was proposed based on ePDF analysis of the amorphous structure (Borisenko *et al.*, 2009b). The analysis of ePDFs of nitrogen-doped Ge–Sb–Te glasses showed that nitrogen predominantly bonds to germanium, and that the increase of the nitrogen content also increases contribution of rings with homopolar bonds (Borisenko *et al.*, 2009a). Carbon-doped Ge–Sb–Te glasses demonstrate the formation of atomic scale carbon clusters coordinated by germanium atoms (Borisenko *et al.*, 2011).

As the medium-range order has a significant effect on the physical behavior of the material (Pagon *et al.*, 2010; Bassiri *et al.*, 2011, 2013; Yan *et al.*, 2012; Hart *et al.*, 2016), studies of fine details of amorphous structures were triggered with the development of a dedicated method – Fluctuation Electron Microscopy (FEM), which demonstrated the paracrystalline nature of amorphous silicon (Borisenko *et al.*, 2012; Treacy & Borisenko, 2012).

Ishimaru (2006) demonstrated the importance of energy filtering for the PDF analysis: the unfiltered data of amorphous SiC showed a significantly different behavior for Q below 10 $\mathring{A}^{-1}$, while the high-Q regions of filtered and unfiltered data were the same (energy slit used was 20 eV). As a result, the unfiltered PDF showed modified intensities, yet the positions of the peaks were not changed, and allowed the assignment of Si–C, as well as C–C and Si–Si distances.

As a reliable method of structure characterization, ePDF could now be applied to a new class of materials – the materials of geological origin. These samples are in most cases multiphasic; therefore, benefitting most from a characterization technique that can address different nano-regions individually. ePDFs of the amorphous component in volcanic glasses (obsidian and pumice) showed a well defined signature of a silicate glass, yet with different fine details in the atomic structure. The arrangement of SiO_4 tetrahedra in the pumice glass was related to the cristobalite and tridymite-type structures (Kovács Kis *et al.*, 2006a). The ePDF analysis of soot particles of different origin showed that some materials consisted mainly of small aromatic moieties, while others were more aliphatic in nature with a small number of conjugated rings (Kis *et al.*, 2006b).

The investigation of the crystallization behavior of amorphous Ag–Cu layers showed the two-stage process with the first stage being the spinodal decomposition of the alloy (Chen & Zuo, 2007). The amorphous phase had a set of peaks in ePDF corresponding to the local atomic arrangement. The formation of different crystalline phases was clearly observed through the splitting of the peaks of the separate phases.

The analysis of ePDFs is the core of ultrafast electron nanocrystallography (Ruan *et al.*, 2009; Farrow *et al.*, 2010); RMC modeling supported the interpretation of gold nanocrystals melting, allowing the melting and re-solidification fronts to be traced, and the formation of an intermediate phase in the graphite-to-diamond transformation process. Many more applications of ultrafast electron diffraction can be found in the review by Zewail (2006).

ePDF was shown to be an excellent tool to study the amorphous to nanocrystalline structure evolution; it was demonstrated that the temperature-induced crystallization of amorphous MgF_2 goes through the formation of the intermediate fluorite-type structure, which then finally converts to the rutile-type crystalline lattice (Mu *et al.*, 2013). The crystallization behavior of amorphous mixed-cation fluorides showed that depending on the atomic composition and stoichiometry, different intermediate structures and different final product can be achieved (Mu *et al.*, 2014). Lattice distortions and disordered states in diverse battery materials are good

candidates to be studied by ePDF; the disordered olivine phase was shown to have the *Pnma*-type structure with the mean correlation domain size of 6 Å (Zhu *et al.*, 2014). A detailed ePDF study of the cycled Mg-based MoS_2-host battery system allowed the 2H–1T phase transformation and a direct observation of the organic cluster signature in the ePDF (Li *et al.*, 2008).

Because of their electron beam stability, mostly inorganic materials are studied by ePDF. However, the moderate electron dose rate conditions realized in an electron diffraction experiment allow the scattering data collection from beam-sensitive organic materials. A study on ePDF calculation from a few organic pigments was reported by Gorelik *et al.* (2015).

A very impressive application of ePDF was recently published (Hristova-Vasileva *et al.*, 2018) which demonstrated the phase separation in amorphous non-stoichiometric Si—O layers. The electron radiation-induced transformation resulted in the formation of amorphous Si clusters encapsulated within an amorphous $SiO_{1.8}$ matrix. The careful analysis of the PDF curves prior to and after the irradiation showed an additional signal originating from amorphous silicon clusters.

Amorphous materials often show features of a certain crystalline phase. Amorphous iridium oxide was shown (Willinger *et al.*, 2017) to have the local arrangement of crystalline hollandite, which allowed conclusions to be drawn about the structural motifs responsible for the high catalytic activity of the material in water-splitting processes.

First attempts of the quantitative treatment of ePDFs showed that multiple scattering can be a serious obstacle (Abeykoon *et al.*, 2012). Electron scattering data collected from 100 nm gold particles with 200 kV electrons showed a significant intensity redistribution in the form of an effective shift of the scattering intensity towards high-Q regions. The elastic mean free path of electrons in gold is 13 nm, which is way below the particle size used, thus ensuring the multiple scattering regime. The elastic mean free path was calculated for gold using the formalism presented in the dedicated section (see below) to be 8 nm at 100 kV ($\lambda = 0.0370$ Å), 13 nm at 200 kV ($\lambda = 0.0251$ Å), and 16 nm at 300 kV ($\lambda = 0.0197$ Å). The intensity distribution in the PDFs was refined using a general damping function Q_{damp}. The refinement of the atomic displacement parameters produced values that were too low, suggesting that a special instrumental effect must be present in the PDF peak width for electrons. The analysis of scattering data from NaCl crystals introduced a new problem: the preferred orientation in the sample due to the crystal habit (Abeykoon *et al.*, 2012). A more systematic approach was presented by Abeykoon and co-workers (Abeykoon *et al.*, 2015), where the same samples were measured using both synchrotron and electron irradiation. This allowed some structural parameters to be fixed during the refinement procedure. Additionally, samples with much smaller particles were used (10 nm gold nanoparticles), thus ensuring the single scattering mode. Again, a general damping parameter Q_{damp} was used to model the PDF intensity decay, the shape of the peaks was modeled by a combination of several parameters: the atomic displacement parameter U, the peak broadening

parameter Q_{broad}, and the peak sharpening parameter δ_2. The refinement quality improved, and the residual factor converged down to 18%.

Given the empirical nature of the correction steps used in the ePDF calculation from the electron diffraction intensity, it is important to see how far the quantitative interpretation of the ePDF can go. The usual procedure for X-ray and neutron PDF analysis is to refine a model in which the structural and instrumental contributions are partitioned. The instrumental contribution for electron diffraction will obviously be different for different TEMs; moreover it can appear different for different experimental geometries such as beam convergence, camera length, accelerating voltage *etc*. A systematic study of the effect of these parameters on the data would be very welcome.

In this paper we outline the main steps necessary to perform in order to obtain the ePDF and describe the influence of relevant effects. Finally, we demonstrate the refinement of a model to ePDF data of nanocrystalline anatase performed in combination with a synchrotron measurement.

2. The amorphous state

Disorder in the form of vacancies, interstitial atoms, impurities, dislocations, grain boundaries and other surface related defects is a natural attribute of a real crystal. In many cases, these defects even determine the physical properties of the bulk material. The idea of a crystal structure can be invoked when the atoms sit on a periodic lattice, *i.e.* long-range order (LRO) exists, with defects considered as a perturbation of the ideal lattice. In some cases, a simple model of disordered or amorphous material can be considered as a case where the defect density has risen to the point where the periodic lattice is lost entirely.

Analogous to an ideal crystal, one can speak of an ideal amorphous solid (Stachurski, 2013). The ideal amorphous solid is defined as a structure with the absence of long-range periodicity; any arbitrary vector that passes through atoms will meet atoms at irregular intervals forming a random sequence. In reality, however, the ideal amorphous structure is as 'rare' as the ideal crystalline structure. In real materials, the strong interatomic forces place atoms at a certain distance from each other, chemical bonds often have a directional nature, so that the angle between the bonds is fixed, and, in fact, the distance to the next-nearest neighbor is defined. The rigid part of the structure given by the chemical bonding in the material is called short-range order (SRO). For a molecular material, the SRO may include the whole molecule (if it is rigid), or if it contains torsion degrees of freedom, the rigid parts of the molecule. The atomic arrangement between the LRO and SRO is loosely defined as medium-range order (MRO), and is often the primary target for characterizing a disordered material.

Amorphous materials with the same chemical composition can have significantly different structures reflected in their MRO. These materials can have different densities, different crystallization behavior (Andronis & Zografi, 2000; Demirjian

et al., 2001), *etc*. Polyamorphism is usually associated with molecular materials and has a potential effect on different crystallization pathways (Machon *et al.*, 2014). Water is a typical molecule showing polymorphic and polyamorphic behavior (Mishima, 2010). In recent years with the growth of interest in the molecular amorphous state (Rams-Baron *et al.*, 2018) more examples of polyamorphism have been reported (Hancock *et al.*, 2002).

The interest in amorphous materials was triggered by amorphous silicon, which showed outstanding performance in solar-cell applications (Stuckelberger *et al.*, 2017) depending on the different content of H-terminated bonds, which in turn has a great effect on the structure (Elliott, 1989).

In recent years the field of amorphous materials has welcomed newcomers such as organic glasses (Gujral *et al.*, 2018), optically active molecular amorphous materials (Murawski *et al.*, 2018), two-dimensional amorphous materials (Huang *et al.*, 2012, 2013) and hybrid organic–inorganic networks, providing even more flexibility in designing their physical properties (Burg *et al.*, 2017).

3. Models of amorphous materials

For many disordered solids, the structure can be represented as a network of polyhedra sharing vertices. This is the case for most inorganic oxide glasses. Zachariasen (1932) proposed a simple method to build a model of an oxide glass based on a few simple rules: (1) an oxygen atom is linked to not more than two atoms A; (2) the number of oxygen atoms surrounding atoms A must be small; (3) the oxygen polyhedra share corners with each other, not edges or faces; (4) at least three corners in each oxygen polyhedron must be shared. The fourth rule brings the third dimension into the model. Although being a very simple construction, this method retained its usefulness up to now, as most models of oxide glasses, such as SiO_2, are created using the *continuous random network* (CRN) model.

Another approach to build an amorphous solid is to use a *sphere packing model* (Stachurski, 2013). Several rules define the behavior of the spheres such as their interaction with the neighbors, 'softness' of the spheres, which enable a wide range of models to be created. Metallic glasses were first reported in 1960 (Klement *et al.*, 1960), showing the utility of the sphere-packing model and generating a new direction in the modeling of amorphous solids. Metallic glasses are believed not to have directional interactions, and thus, only the size and the nearest coordination of the different metals constituting the sample define the structure of the material. Yet, it was shown experimentally that some materials can have a hidden order in the MRO region, which is responsible for different packing in crystalline structures (Wu *et al.*, 2015; Zeng *et al.*, 2011). This required modification of the simple models (Yue *et al.*, 2017). Different amorphous states can be realized for metallic glasses, thus we can talk of polyamorphism in these materials (Sheng *et al.*, 2007).

3.1. Molecular dynamics (MD)

MD is an efficient way to simulate the physical movements of atoms and molecules (Fig. 1). In principle, the MD method is an iterative numerical scheme for solving a set of motion equations, which represent the physical evolution of the system under study. The MD approach was introduced in the late 1950s by Alder and Wainwright (1957, 1959) for the calculation of the interaction between hard spheres, but it was many years later that the method became practically relevant, supported by adequate computer facilities. MD simulations are not only applied to inorganic glasses, but also are essential for molecular materials (Ou & Chen, 1998). In MD simulations, the trajectories of all particles in a system are calculated by integrating the laws of motion and the total energy of a system is the sum of several energy terms/contributions. The forces acting on each particle are derived from an interatomic interaction potential (forcefield). Usually one distinguishes between classical and reactive forcefields, where the latter ones are capable of mimicking bond order formation and dissociation processes, thus simulation of entire reaction mechanisms. A more detailed description of the potential terms and the energy terms is given by Chenoweth *et al.* (2008).

Based on obtained MD trajectories one can deduce the PDF of a particular system, which also allows analyzing its dynamic behavior as well as dependence on environmental parameters (*e.g.* temperature, pressure, *etc.*).

3.2. Reverse Monte Carlo (RMC)

RMC is another widely used method of structural modeling based on fitting experimental data (either in direct space in the
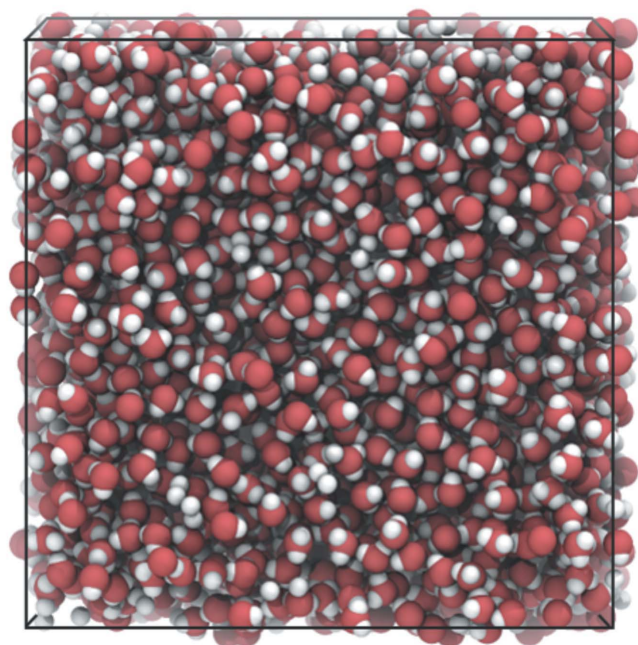

Figure 1
MD model of water used for PDF calculations.

form of PDF or in reciprocal space in the form of diffraction) to simulated data from a trial model (McGreevy & Pusztai, 1988; Eremenko *et al.*, 2017). The model is initially created as a set of atoms in a box under periodic boundary conditions, which are allowed to move. After each move, the fit to the experimental data is calculated. If the fit is improved then the move is accepted unconditionally, otherwise it is accepted with a certain (low) probability depending on the fit match.

The RMC strategy is particularly attractive for modeling of disordered or amorphous materials. The PDF of amorphous materials only consists of a few peaks, making the number of observables very low in contrast to the number of refined parameters (several thousand atomic coordinates). In this case a wise choice of constraints is essential to obtain a reasonable structural model. Typical constraints imposed on atomic configurations are connectivity, bond length and bond angles, and the formation of certain ring structures, observed for instance by an independent NMR experiment or suggested by density functional theory (DFT) simulations. The interpretation of the final model should be made with regard to the constraints used.

RMC simulations were often performed in combination with ePDF and DFT simulations (Borisenko *et al.*, 2009*b*, 2012; Pagon *et al.*, 2010; Bassiri *et al.*, 2011, 2013) to deliver structural models.

Amorphous materials often possess SRO which is similar to that found in known crystallographic structures of similar compounds, and can be modeled using the periodic structure which is modified by damping functions and increased atomic displacement parameters (ADPs). This approach is called '*small box modeling*', and it has an obvious benefit of having only a few parameters rather than hundreds, otherwise needed for amorphous materials. This strategy is often used in X-ray and neutron PDF refinement (Petkov *et al.*, 1999; Nakamura *et al.*, 2017; Transue *et al.*, 2019), and will certainly be efficient for ePDF analysis.

4. PDF as a structure fingerprint

In the presence or absence of translational periodicity, the structure can be described by the atomic pair distribution function (PDF). In a system of atoms, the PDF describes the variation in atomic density as a function of distance from a reference atom. In the simplest terms, the PDF is a measure of the probability of finding an atom at a distance *r* from a given atom. The PDF is usually normalized with respect to the average, uncorrelated atomic density (Egami & Billinge, 2012). The common variables used to describe the correlations are:

f_i is the scattering power of atom *i*,

$f_i(0)$ is the scattering power of atom *i* at the scattering momentum transfer position 0,

r_{ij} is the scalar distance between two atoms *i* and *j*,

N is the total number of atoms in a sample,

ρ_0 is the number density of atoms,

ρ is the atomic pair distribution function, and

γ_0 is the baseline effect due to domain shape (Farrow & Billinge, 2009).

In real space, the atomic PDF can be easily calculated from a structure model, as implemented in many current softwares, to be discussed later. The process can be understood in terms of the radial distribution function, $R(r)$, which describes the average number of atoms located in a spherical shell at a distance *r* away from any atom at the origin, defined as

$$R(r) = \frac{1}{N\langle f(0)\rangle^2} \sum_i \sum_j f_i(0)f_j(0)\delta(r - r_{ij}). \tag{1}$$

Because the number of atoms at a given distance scales with the area of the spherical shell, the function scales as $4\pi r^2$. The atomic pair density function can be obtained from $R(r)$, by first normalizing by the surface area of the spherical annulus associated with a given radial distance, and then the average number density, giving

$$g(r) = \frac{R(r)}{4\pi r^2 \rho_0}. \tag{2}$$

Using this formalism, as *r* goes to infinity, $g(r)$ goes to 1 which represents the average number density, and as *r* goes to 0 (smaller than the shortest interatomic distance), $g(r)$ goes to 0. In most cases, it is more practical to use the reduced pair distribution function which is obtained directly from the experiment, given by

$$G(r) = 4\pi r\rho_0\big[g(r) - \gamma_0\big]. \tag{3}$$

In this case, the resulting $G(r)$ function oscillates around 0 at large *r*, and at low *r* it behaves like $4\pi r\rho_0\gamma_0$ where γ_0 is a nonlinear component to the baseline which comes from the shape for nanosized domains (Farrow & Billinge, 2009). Other definitions of the PDF exist and typically vary by the normalizations considered (Keen, 2001). It should be clear that in the cases described, the peak intensity at a given *r* value depends on both the number of pairs separated by that distance, and the relative scattering powers of the atoms contained in any given pair. The atomic scattering factors $f(Q)$ are tabulated (Prince, 2004) and are functions of the scattering vector. In PDF analysis, the scattering vector is usually measured in Q, which is related to the reciprocal distance as follows:

$$Q\ (\text{Å}^{-1}) = (4\pi \sin\theta)/\lambda = (2\pi)/d. \tag{4}$$

The electron scattering factor for a single atom is proportional to the Fourier transform of the Coulomb potential of the atom FT[$V(r)$] (Reimer & Kohl, 2008):

$$f(q)\ (\text{Å}) = \frac{m_e e}{2\pi\hbar^2}\text{FT}[V(r)]. \tag{5}$$

Here, m_e is the electron mass, *e* is the electron charge and $\hbar$ is Planck's constant. While Q-dependent scattering factors must be used to normalize the raw diffraction data, for practical reasons, PDFs simulated from structure models in real space use only the values of the scattering factors at $Q = 0f_i(0)$.

Fig. 2 shows the electron atomic scattering factor curves for oxygen (blue), hydrogen (black) and the average scattering amplitude for water molecule calculated as

$$f = \tfrac{1}{3} f_{oxygen} + \tfrac{2}{3} f_{hydrogen}. \qquad (6)$$

The values for the atomic scattering factors at zero momentum transfer (Rez *et al.*, 1994) are 1.983 Å for oxygen, 0.529 Å for hydrogen and 1.499 Å for water molecule average scattering.

5. How to *read* a PDF

The physical sense of the PDF is demonstrated here for water molecules. A model of liquid water at 0°C containing 3046 molecules was produced using MD simulations (Fig. 1). The force field used here is self-created and has been extensively tested. It takes polarization of the molecules into account.[1] For comparison, a PDF was calculated for the Ih (ordinary) crystalline ice (Kuhs & Lehmann, 1983). The PDFs are shown in Fig. 3.

5.1. Peak position[2]

The PDF describes the probability of finding a pair of atoms separated by a certain distance. For the water molecules (Fig. 3), the first peak in the PDF at the interatomic distance below 1 Å corresponds to the length of the O—H covalent bond. The weak peak at 1.5 Å comes from the two hydrogen atoms of the same water molecule. The broad peak shortly before 2 Å corresponds to the oxygen to hydrogen distance of two adjacent molecules connected by a hydrogen bond. The strong peak before 3 Å originates from the first oxygen–oxygen distance and represents the first solvation shell. For water molecules, the SRO ends here; before 3 Å the PDFs of crystalline ice and liquid water look similar. From this point on a different character of the MRO in the solid and liquid phase creates differences in the PDFs. For the crystalline structure, the MRO is composed of well resolved peaks, whereas for the liquid phase only a few broad peaks at 4.5 Å and 7 Å can be recognized. The peak at 4.5 Å also exists in the crystalline packing and comes from the second O–O distance; thus forming the second 'solvation shell' in Ih ice. Thus, it is probably associated with the second solvation shell in the

[1] In this work we use the ReaxFF potential (Van Duin *et al.*, 2001; Fantauzzi *et al.*, 2014), which is based on the bond order/length ratio introduced by Abell (1985). A more detailed description of the potential and the energy terms are given by Chenoweth *et al.* (2008). The calculations presented in this work have been carried out for periodic systems, *i.e.* assuming the liquid phase condition. The system in this study was prepared as follows: first, water molecules were placed inside of a square box with 45 Å edge length. The system was then optimized using the conjugate gradient algorithm with an endpoint criteria for energy minimization of 1.0 kcal mol^{-1}, followed by an *NVT* (a system with constant number of particles *N*, volume *V* and temperature *T*) velocity Verlet algorithm dynamics at various temperatures, employing the Berendsen thermostat (Berendsen *et al.*, 1984) with a coupling constant of 100 fs. Four hundred thousand iteration steps as equilibration (0.25 fs time step) were followed by 40 000 iterations saving the position and velocity of every atom at every 5 000 time steps.

[2] The accuracy of peak positions in the PDF is related to the accuracy of the camera length calibration of the transmission electron microscope. The manufacturer's specifications for the camera length accuracy are typically about 2%; however, in many cases a better accuracy can be reached.
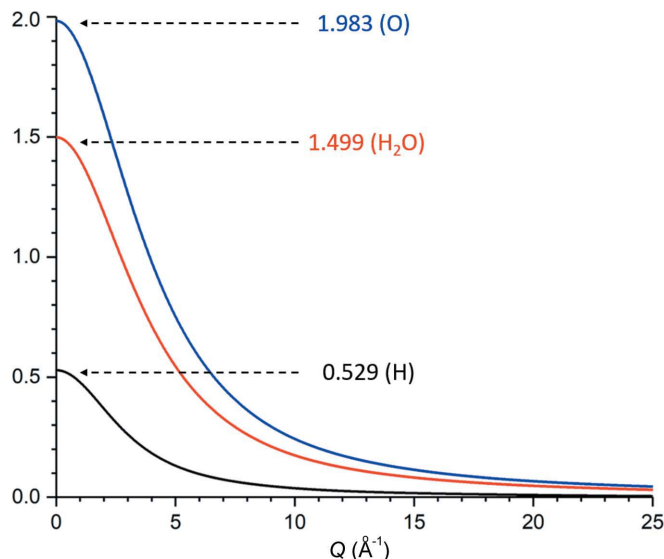

Figure 2
Atomic scattering factors for electrons for oxygen (blue), hydrogen (black), a combined scattering factor or a water molecule (red), and the values for *Q* = 0, of oxygen hydrogen and water molecule, respectively.
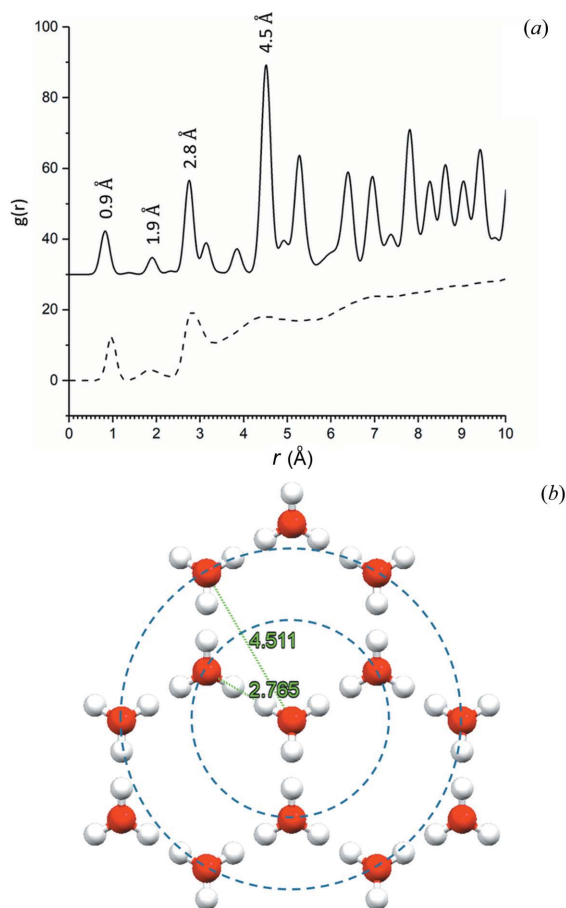

Figure 3
(*a*) Simulated PDFs for crystalline (Ih) ice (solid line) and liquid water at 0°C (dashed line). (*b*) A fragment of Ih ice crystal structure is presented showing schematically the first and the second solvation shells.

liquid phase. Although, the interpretation of the following 7 Å peak is not this trivial, one can state that the maximal correlation distance for the liquid structure reaches at least 7 Å. No oscillations in the PDF are seen from this point on.

5.2. Peak intensities

The intensity of a peak in a PDF is the coordination number in the shell weighted by the mean scattering power of the two

Figure 4
TEM images of the gold particle samples used for electron diffraction data; (*a*) the smallest particles (the average particle diameter is about 4 nm), (*b*) the medium particle diameter of about 8 nm, and (*c*) the largest particles are of 20 nm in diameter. Azimuthally integrated experimental scattering intensity profiles (*d*) for the 4 nm particles (red), the 8 nm particles (green), and the 20 nm particles (blue) (a simulated powder diffraction pattern of nanocrystalline gold is shown in black for comparison), and (*e*) the corresponding reduced structure functions $F(Q)$ obtained through the normalization of the scattering profiles to the atomic scattering factor of gold and subtracting of a polynomial background in order to improve the asymptotic behavior of the $F(Q)$. Reduced PDFs of nanocrystalline gold powders (*f*): the 4 nm particles (red), the 8 nm particles (green), and the 20 nm particles (blue). A simulated (*DISCUS*; Proffen & Neder, 1999) PDF of a 2 nm spherical gold particle is shown for comparison in black.

atoms contributing to the signal. This explains for instance why the peak at 1.5 Å in the ice PDF is very weak (Fig. 3) (it reflects the distance between two hydrogen atoms) and therefore is weighted by the low scattering power of H. The coordination numbers can be estimated from the PDF directly: the distance associated with the first solvation shell is close to 3 Å. In the crystalline structure (solid line) the coordination is 4; in the liquid phase the corresponding peak is broader, suggesting a certain distribution of the distances, but the integral value of the peak also approaches 4.

5.3. Overall peak intensity decay

For an ideal crystal, the probability of finding atomic pairs at a specified distance will oscillate infinitely. As a result, the peaks in a PDF will be seen up to very large interatomic distances. These peaks will probably overlap and will be difficult to interpret. When the crystallite size is limited as in the case of the gold particles (Fig. 4), the probability of finding atomic pairs at a distance exceeding the size of the cluster will be equal to zero. As *r* approaches the size of the cluster, the intensity of the peaks will decay. The form of the crystallite-size damping function depends on the size and the shape of the particle, in addition to any size or shape distribution over all particles in the sample. The situation is somewhat different for an amorphous model, *e.g.* in the PDF of water (Fig. 3, dashed line), the probability of finding atomic pairs at long distances becomes indistinguishable from the average number density; thus giving a flat line at distances beyond any signal present from LRO and MRO.

Due to the nature of the Fourier transformation, representing the core of the PDF calculation, the overall intensity decay in the PDF is a result of Bragg-spot width in electron diffraction patterns, which further determines Debye–Scherrer ring widths for orientationally averaged measurements. The diffraction spot width is in turn a combination of the structure-induced broadening and instrumental broadening introduced by electron optics focusing and, not the least, the point-spread function of the recording medium. It is very difficult to separate the instrumental and the structural contributions.

5.4. Peak width

The peak width is related to the experimental parameter Q_{max}, not relevant in the calculation presented above, and the spread of atomic distances for a given structure, related to the crystallographic thermal factor.

In the case of water, it is evident that the first two peaks are rather sharp compared to the following peaks. The first two peaks describe the intramolecular interatomic distances within a single molecule. The following peaks correspond to intermolecular distances. In the model, the molecule has a rigid geometry; thus, the distances within the molecule are well defined. The intermolecular distances have a broader distribution, which is reflected by the corresponding increase in the width of the peaks at these distances.
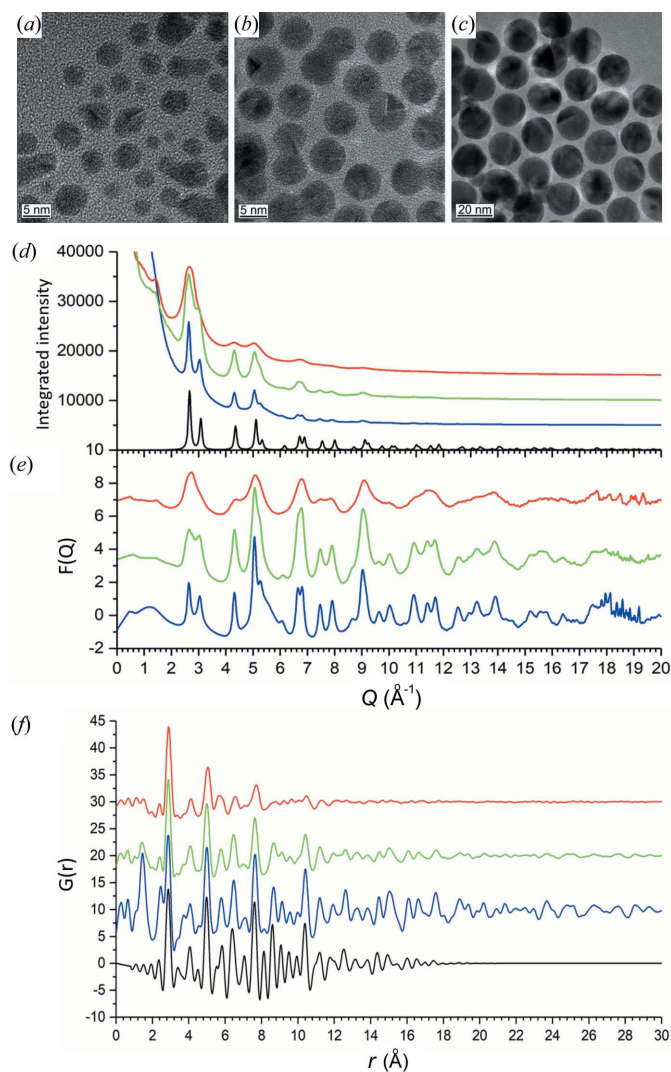
A similar effect has been observed for molecular crystals. The thermal vibration of atoms belonging to one molecule usually has a smaller amplitude than the thermal vibration between different molecules, and is better described with a smaller effective thermal factor (Prill *et al.*, 2015).

6. Experimental PDF

The PDF can be obtained experimentally from powder diffraction data. Azimuthal integration of a 2D powder diffraction pattern results in a scattering intensity profile $I(Q)$. The obtained intensity profile must go through certain corrections – typically a multiplicative correction in the form of normalization to the average scattering factor of the sample $f(Q)$, and an additive correction, which in most cases polynomial background subtraction is used (Mu *et al.*, 2013). The result of these corrections is the total scattering structure function $S(Q)$. The reduced structure function $F(Q)$ is calculated as follows:

$$F(Q) = Q[S(Q) - 1]. \qquad (7)$$

The reduced pair distribution function $G(r)$ is then calculated through a sine Fourier transform:

$$G(r) = \frac{2}{\pi} \int_{Q_{min}}^{Q_{max}} F(Q) \sin(Qr) dQ. \qquad (8)$$

Fig. 4(*d*) shows integrated electron diffraction scattering profiles of nanocrystalline gold powders. The three samples [Figs. 4(*a*)–4(*c*)] had different particle sizes: small (around 4 nm), medium (8 nm) and large (20 nm). The difference in the particle size is reflected in the peak width in the corresponding diffraction patterns [Fig. 4(*d*)]: the red profile with the broad peaks represents the 4 nm gold particles, whereas the blue profile with the narrow peaks corresponds to the 20 nm particles. The black profile shows the simulated diffraction profile of the nanocrystalline gold. As particle size decreases, the Bragg peaks broaden and merge.

Fig. 4(*e*) shows the reduced structure functions $F(Q)$ calculated for the scattering profiles shown in Fig. 4(*d*). The width of the Bragg peaks shows the same tendency as for the intensity data. One can see that at high scattering vectors, the structural information vanishes, and the profiles are dominated by noise. Here, no structural information seems to be in the data after $Q = 17$ Å^{-1}. The sharp features beyond 17 Å^{-1} seen in $F(Q)$ [Fig. 4(*e*)] are artifacts of the low-intensity data integration at high scattering momentum transfer. It is therefore feasible to truncate the data there before calculating the $G(r)$. It is often sensible to truncate the data because of the systematic errors, even if there is structural information beyond this range. The region of low Q (below 2 Å^{-1}) contains effects from the primary beam, and should also be excluded from further calculations. Although truncating the data in this region will produce very low frequency oscillations in the PDF, they are typically very weak with little effect on the structural refinement.

The reduced PDFs for these samples are shown in Fig. 4(*f*). The red profile corresponds to the particle size of 4 nm, the green to 8 nm, and the blue PDF is calculated for the 20 nm particles. The calculated mean free path of electrons at 300 kV in gold is 16 nm; thus, the first two samples represent fully single scattering mode, while the last sample with 20 nm particles already includes multiple scattering effects.

One can see that the PDF of the large particles shows oscillations going further out (blue), when compared to small particles (green and red). Yet the longest correlation distances seen in the PDFs do not correspond to the largest particle sizes. For the largest particles, this is primarily due to damping as a result of the limited instrumental resolution. However, further damping of the signal in the smaller particles, below the instrumental resolution, can be explained by the presence of multiple incoherent domains in the particles. The presence of stacking faults can lead to new interdomain distances in the PDF, but if the domains are not symmetrically related around the boundaries, then severe overlap and broadening of these interdomain distances may occur; the effect of twin planes on the PDF was recently demonstrated (Banerjee *et al.*, 2018), also seen in the TEM images [Figs. 4(*a*)–4(*c*)]. From the PDFs it follows that the particles of 4 nm have an average crystal size of 15 Å, the 8 nm particles are 30 Å, and the 20 nm particles are above 50 Å. No instrumental resolution was considered here, so we cannot estimate the domain size from the 20 nm particles.

The black profile at the bottom of Fig. 4(*f*) is a simulated pattern of a spherical 2 nm gold crystal. Comparing the sequence of the peaks in the experimental and the simulated
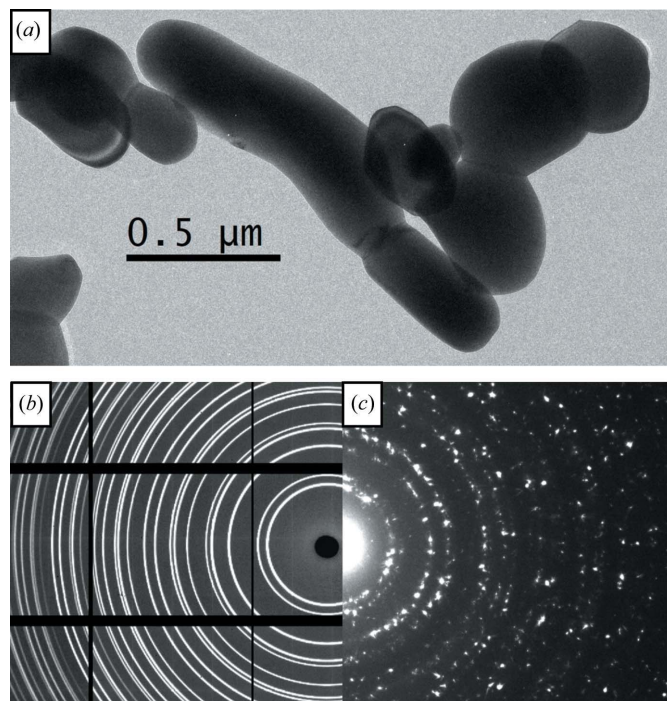

Figure 5
NIST ceria sample: (*a*) TEM image of the cerium oxide crystals, (*b*) synchrotron powder diffraction pattern and (*c*) electron diffraction pattern.

PDFs, one can see that these match pretty well. As seen from the TEM images shown in Figs. 4(a)–4(c), the samples, especially the one with the smallest particles, have broad size distributions; besides nanocrystalline gold is known to contain multiple twins. We therefore, refrain from quantitative interpretation of the PDFs here. The blue PDF (20 nm particles) shows two additional peaks at low r at 1.4 Å and 2.5 Å. These peaks originate from the structure of the supporting carbon film. The smaller contribution of these peaks is also seen in the green and the red PDFs. In the sample area used for the diffraction pattern acquisition of the large particles, only a few particles were present, so the volume fraction of the carbon support is relatively large.

7. Electrons versus X-rays – different target scales

The nature of the interaction of electrons with materials is rather different compared with that of X-rays. As a result, electron diffraction can address very small volumes. At the same time, it can struggle with materials which are otherwise standard for X-ray analysis. Nanocrystalline ceria[3], a standard sample for the calibration of X-ray sources can hardly be addressed by electron diffraction (Fig. 5). The crystals are rather large, so that even for electron diffraction geometry with a relatively large sample area, no perfect statistical averaging and continuous intensity distribution along the rings can be achieved. Secondly, the relatively large particle size in combination with the presence of the strong scattering elements gives rise to strong dynamical scattering effects, seen here as an irregular reflection shape.

The ability of electrons to give a substantial scattering signal from small volumes can be very beneficial for amorphous materials. In 2005, Treacy *et al.* suggested the idea of Fluctuation Electron Microscopy (FEM), which is based on a systematic scan of the sample in diffraction mode with a relatively small electron beam of a few nanometres. A systematic analysis of the variance of the patterns recorded at different sample positions allows conclusions to be drawn about the homogeneity of the bulk-amorphous substance. FEM is an excellent technique to detect the modulations of the MRO because of its application as a local probe. These fluctuations cannot be seen in a typical PDF measurement, which is instead a bulk average probe of the local structure in the sample. So, the view on amorphous silicon completely changed recently with a report on a paracrystalline structure with a local ordering on the 10 to 20 Å length scale (Treacy & Borisenko, 2012).

With the recent advances in electron optics, tiny coherent electron beams can be produced which can focused down to a few Ångströms. The scattering of electrons from using the Ångström-size beam allowed the very local atomic environment in metallic glasses to be probed (Hirata *et al.*, 2011). This

information was used to reconstruct the nearest atomic arrangement and propose different SRO clusters present in glass (Hirata *et al.*, 2013).

8. Dynamical scattering in electron diffraction and ePDF

Due to their strong interaction with matter, electrons are likely to scatter multiple times on their path through the sample. In diffraction, multiple scattering causes a redistribution of diffraction intensities in such a way that the experimental intensity at high scattering angles is much higher than the kinematically calculated values (Anstis *et al.*, 1988). This results in a deviation of the experimental diffraction profile from the theoretical *single atomic scattering factor* which is used as a normalization in ePDF analysis of experimental diffraction. As a result, the coordination numbers are commonly underestimated in the quantitative analysis of the experimental ePDF (Mu, 2013; Mu *et al.*, 2013).

For 3D isotropic amorphous structure, it is generally accepted that subsequent scattering events along the electron path are independent of each other. It implies that multiple
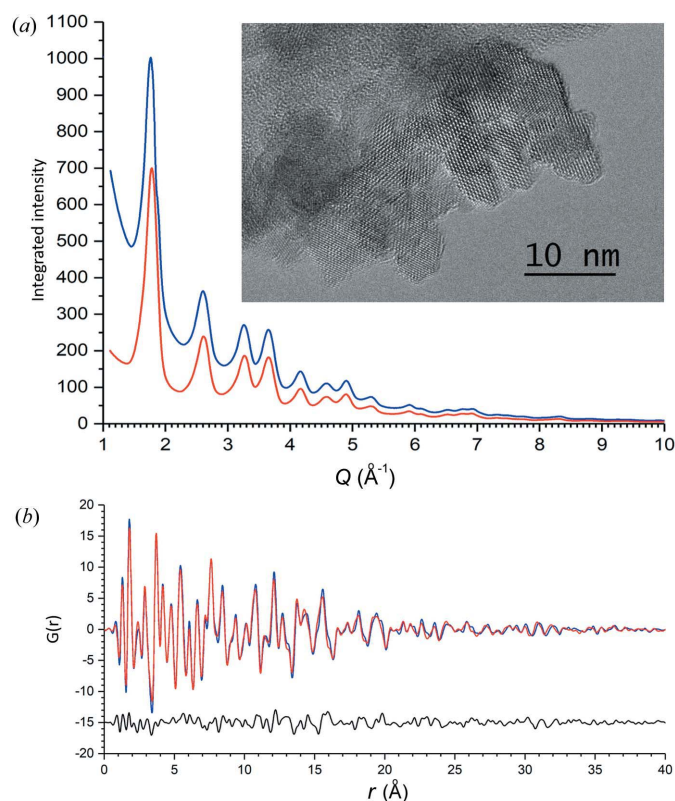

Figure 6
(a) Electron scattering for nanocrystalline anatase at 300 kV, room temperature data with (red) and without (blue) zero-loss energy filtering. Energy slit width is 10 eV. Insert: high-resolution TEM image of the nanocrystalline anatase sample. (b) Electron PDFs of nanocrystalline anatase for zero-loss energy filtered (red), unfiltered (blue) diffraction data, and the difference curve, off-set below (black). Q_{max} 17 Å^{-1}, 300 kV, energy slit 10 eV.

---

[3] NIST ceria sample 674b with the specified average crystallite size 380 nm. Synchrotron data measured at ESRF ID31 beamline on a Dectris CdTe detector, electron diffraction data: TITAN, 300 kV, nano-diffraction mode with the beam diameter of 5 mm, GIF Gatan MSC 2k CCD, zero-loss energy filtering, slit width 10 eV.

electron crystallography

scattering in amorphous materials can be accounted for by a simple convolution as

$$I_k(\mathbf{Q}) = [I_1(\mathbf{Q}) \otimes I_1(\mathbf{Q}) \otimes \ldots I_1(\mathbf{Q}) \otimes]_{k\text{-times}}, \qquad (9)$$

where $I_k(\mathbf{Q})$ is the intensity distribution of k-times scattered electrons, $\mathbf{Q}$ is the scattering vector, $I_1(\mathbf{Q})$ is the purely kinematical (single-time) scattering intensity distribution. A Fourier log deconvolution method can be adopted to retrieve the single-scattering signature (Ankele *et al.*, 2005).

A deconvolution of experimental diffraction from a 35 nm-thick NiO polycrystalline thin film showed a 3× overestimation of the coordination number in the PDF analysis (Mu, 2013). This indicates that the convolution scenario does not match the dynamic propagation of electrons in the nanocrystals due to their 3D anisotropic atomic structure. Nevertheless, many recent works show excellent agreement of peak position and shape between the experimental and simulated PDFs of nanocrystalline materials (Mu *et al.*, 2013; Zhu *et al.*, 2014; Li *et al.*, 2008). This provides confidence for applying the ePDF to analyze the interatomic distances, bonding angles and even the relative coordination numbers between peaks in crystalline nanoparticles.

9. Elastic and inelastic scattering of electrons

Electron interaction with matter leads to an avalanche of different processes, classified in different categories, among them elastic and inelastic scattering. Inelastic scattering contributes to a diffraction pattern primarily as background. Fig. 6(*a*) shows integrated electron diffraction patterns for nanocrystalline anatase[4] recorded with (red) and without (blue) zero-loss energy filtering. It is evident that the most significant effect of the energy filtering is the elimination of the background in the data.

For a monoatomic system, the mean free path for elastic and inelastic scattering can be estimated by using the relations $1/[N\sigma(\text{el})]$ and $1/[N\sigma(\text{in})]$, respectively. Here N denotes the number of atoms per unit volume, and $\sigma(\text{el})$ and $\sigma(\text{in})$ represent the elastic and inelastic scattering cross sections for certain kinds of atoms, respectively. We calculate the elastic scattering cross section based on the Wentzel model (Reimer & Kohl, 2008):

$$\sigma_n(\text{el}) = \hbar^2 Z^{4/3} / \pi E_0^2 \beta_2. \qquad (10)$$

Here $\hbar$ represents Planck's constant; Z is the atomic number; $\beta = v/c$ is the ratio between the electron velocity v and the speed of light c; E_0 is the energy of the atom at rest, calculated by $m_0 c^2$ with m_0 denoting the rest mass of the atom. The inelastic scattering cross section is obtained by employing the empirical relation (Reimer & Kohl, 2008):

$$\sigma(\text{in}) = 20\sigma(\text{el})/Z. \qquad (11)$$

For a composite structure, its effective atomic number is estimated by applying the relation $Z_{\text{eff}} = \Sigma f_n Z_n$. Here, f_n is the

---

[4] Nanocrystalline anatase sample with the nominal crystal size of 5 nm was purchased from Nanostructured & Amorphous Materials, Inc., Katy, TX, USA.

Table 1
Experimentally determined ratio of elastic to inelastic contribution for nanocrystalline (5 nm) anatase.

The theoretically predicted ratio is 1.5, constant for different voltages.

	300 kV, $\lambda = 0.01969$ Å	80 kV, $\lambda = 0.04176$ Å
Room temperature	1.6	0.96
Liquid nitrogen temperature	1.4	0.91

ratio of the atoms characterized by the atomic number Z_n. We acquire the elastic and inelastic scattering cross sections of a composite sample by substituting Z in equations (10) and (11) for the scattering cross section with Z_{eff}.

For a composite structure, the mean free paths for elastic and inelastic scattering are estimated by using the relations $1/[\Sigma N_n \sigma_n(\text{el})]$ and $1/[\Sigma N_n \sigma_n(\text{in})]$.

Generally, the mean free paths for both elastic and inelastic scattering increase along with the accelerating voltage. The mean free path corresponding to elastic and inelastic scattering for titanium dioxide is plotted as a function of accelerating voltage in Fig. 7.

One can see that the mean free path decreases as the accelerating voltage drops; as a result, thinner specimens are then needed in order to avoid the multiple scattering regime. Combined data recorded at different voltages can be used to extract single scattering data (Petersen *et al.*, 2005).

The average particle size of the anatase sample is far below the values for the elastic and inelastic mean free paths at accelerating voltages ≥ 80 kV. Thus, only single elastic and inelastic scattering events can take place.

The scattering cross section $\sigma(\text{el})$ for elastic scattering is proportional to the integrated intensity of the corresponding filtered diffraction pattern D_{fil}, and the scattering cross section $\sigma(\text{in})$ for inelastic scattering is proportional to the difference
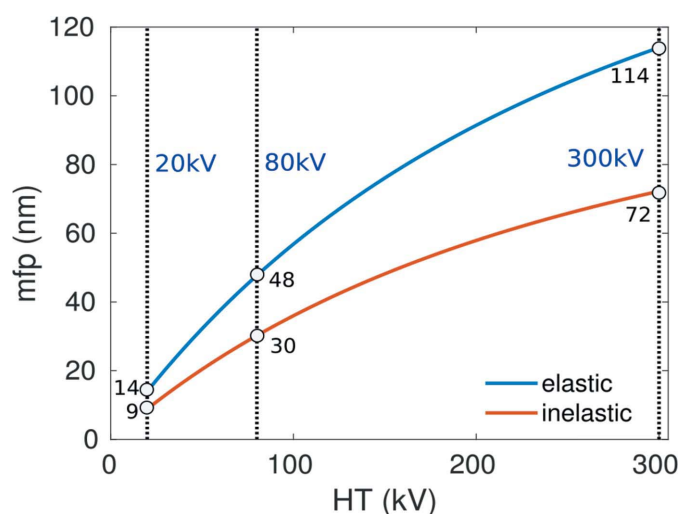

Figure 7
Mean free path (MFP) corresponding to elastic and inelastic scattering as a function of accelerating voltage for TiO_2. The values of the MFP are marked for 20 kV, 80 kV and 300 kV.

$D_{un} - D_{fil}$ between the integrated unfiltered and filtered diffraction patterns. For the integral of both diffraction patterns, the intensity contributed by the unscattered central beam needs to be excluded. Accordingly, the ratio between the mean free paths for elastic and inelastic scattering is obtained by $\lambda(el)/\lambda(in) = (D_{un} - D_{fil})/D_{fil}$.

A summary of the ratio between the experimentally determined amount of elastic and inelastic scattering is presented in Table 1. The ratio obtained from our calculations (Fig. 7) is around 1.6 for the accelerating voltages in the range of 20–300 kV. This behavior is determined by the equation for the cross sections applied in the calculations. At 300 kV, the experimental value matches our calculations very well, while there is still a discrepancy between the experiment and the calculation at 80 kV. This result indicates that it is sensible to add a voltage-dependent factor in the scattering cross section formalism, yet these considerations are far beyond the scope of this work.

To estimate the relevance of inelastic scattering, we calculate PDFs for both zero-loss energy filtered and unfiltered profiles shown in Fig. 6(a). The most evident contribution of the inelastic scattering is eliminated during the background subtraction procedure. The obtained PDFs are shown in Fig. 6(b). Essentially there is no difference between the two functions. Hence, we can conclude that for the case of titanium oxide with the crystal size far below the electron mean free path for inelastic scattering, the influence of inelastic scattering is negligible. As a result, energy filtering does not bring a significant improvement to the PDF quality.

10. Practical issues associated with ePDF

10.1. Data acquisition

Powder electron diffraction patterns can either be collected in nanodiffraction mode with the condenser lens system limiting the beam diameter, or in Selected Area Electron Diffraction (SAED) mode, with the selected area aperture, virtually limiting the area in which electron diffraction data is collected. Image plates are reported to be superior compared with the modern cameras for electron diffraction data collection, yet the read-out and erasing procedures are time consuming, so for practical reasons, most operators prefer to use CCD or CMOS chips.

The diffraction pattern should be collected up to relatively high scattering angles, i.e. using a relatively short camera length. Good X-ray PDFs are usually obtained using Q_{max} values of around 20–30 Å^{-1} ($d = 0.2$ Å), depending on the material, which can be challenging for a transmission electron microscope. However, suitable electron diffraction data can be collected up to a Q_{max} of 20 Å^{-1} ($d = 0.3$ Å).

The diffracted intensity at high scattering angles is very weak; therefore, long exposures may be needed to record data of sufficient quality for Fourier transformation. All uneven features of the background with initially weak intensity can be enhanced during the data collection. Stray scattering, often present in SAED data, makes SAED patterns less attractive

for PDF analysis than the data collected in nano-beam diffraction mode (Lábár et al., 2012).

Modern transmission electron microscopes allow a diffraction pattern to be shifted with respect to the detector. This gives the option to physically exclude the primary beam from the data collection. In this case, the data can be collected at high intensity or long exposure, ensuring a high quality signal at high-scattering angles. The mosaic diffraction data acquisition is particularly attractive for energy-filtered diffraction patterns recorded with a Gatan image filter (GIF). As no full rings are recorded in the mosaic data, special centering routines must be used, which sometimes can rely on a pre-calibration of the diffraction pattern shift (Fig. 8).

All features in the pattern that do not come from the scattering from the sample, such as the beam stop, blooming effects and shutter shadows must be masked out prior to the integration. The diffraction patterns may also need to be corrected for elliptical distortion.

The center of the diffraction pattern must be found as accurately as possible. There are different algorithms for data centering, realized in different programs. Most of them rely on the radial symmetry of the pattern; the center of elliptically distorted patterns and the amount of distortion can also be determined (Lábár & Das, 2017).

10.2. Integration

Once the problematic features are masked out, and the center of the pattern is found, the 2D diffraction pattern can be integrated into a one-dimensional $I(Q)$ scattering profile. There are several programs available for this procedure: *DiffTool*, a plugin for *GMS* (Digital Micrograph Suite, GATAN, USA); Dave Mitchell has developed a number of scripts allowing diffraction data processing and integration into a one-dimensional profile (Mitchell, 2008; http://www.dmscripting.com/); *ELD* (a part of *CRISP*) (CALIDRIS, Sweden; http://www.calidris-em.com/eld.php); *FIT2D* (Hammersley et al., 1996; Hammersley, 2016); *pyFAI* (Ashiotis et al., 2015); *DAWN* (Filik et al., 2017) – the software used for
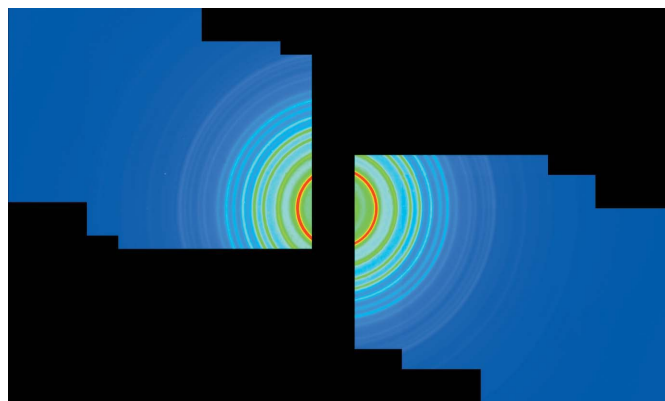
Figure 8
A mosaic diffraction pattern of nanocrystalline anatase, recorded using calibrated diffraction shift.

the X-ray diffraction integration, and the dedicated software for the ePDF calculation (see below).

10.3. Normalization and background subtraction

The average electron scattering factors are calculated as a weighted sum of individual atomic scattering factors (as explained above). Then, the experimental scattering curve is normalized by the obtained $f(Q)$. The experimental scattering profile contains features which cannot be modeled with the $f(Q)$. Most problematic is the low-Q region, close to the primary beam, beam stop, overexposed areas, *etc*. Usually the very low-Q region is excluded. Even then, for most samples, the $S(Q)$ contains low-frequency oscillations, appearing as curve bending, so that additional background subtraction is necessary in order to ensure the proper $S(Q)$, asymptotically oscillating around a straight line. The redistribution of the scattering intensity is believed to be a result of multiple scattering and appears for both amorphous and crystalline materials (see Section 8). The empirical background correction can either be made at this stage using a polynomial function, or at an earlier stage, directly from the experimental scattering profile using a $1/Q$ dependence (this approach is implemented in *SUePDF* (Tran *et al.*, 2017) package.

The main disadvantage of the background subtraction procedure is that the correct atom amount cannot be derived anymore. Accordingly, the absolute scale in the PDF is not known, and, as a result, the coordination numbers can only be determined in relation.

10.4. Fourier transformation

A Fourier transformation is carried out to obtain the PDF from $S(Q)$ using the formula shown above. In $S(Q)$, at high scattering angles, the noise in the experimental data increases and the amount of the structural information decreases. The usual practice is to truncate the scattering data at a certain Q_{max} in order to achieve the best compromise between maximal real-space resolution with minimal possible artifacts in the PDF due to noise. The width of the peak in the PDF is directly related to the value of Q_{max} used for the calculation; the smaller the Q_{max} is, the broader are the peaks in the corresponding PDF.

The truncation of the experimental data unavoidably produces ripples around the peaks with the frequency related to Q_{max}. These ripples can be very strong around strong peaks and be easily misinterpreted as extra structural features. In order to check if the peaks are 'real', it is recommended that several PDFs with different values of Q_{max} are calculated. The positions of the peaks related to the structure will not be affected by this.

11. Refinement on nanocrystalline anatase structure from e-PDF data

Refinement is a general procedure referring to all operations needed to develop a suitable trial model explaining the experimental data and to obtain a quantitative fit of this model

associated with a corresponding figure of merit. In the framework of PDF refinement, the models can be roughly divided into the structural and instrumental contributions to the data. Here, we demonstrate the ePDF refinement of the nanocrystalline anatase sample (Fig. 6).

We intentionally selected a material with a relatively simple structure, without defects of the lattice (*e.g.* stacking faults), and with a relatively narrow particle size distribution. The calculation of electron mean free path in TiO_2 showed that multiple scattering can be neglected for this sample. Thus, the structural parameters are reduced to the mean particle (crystal) size, lattice parameters a, c, one atom position, and a atomic displacement factors for the atoms.

The instrumental contribution is associated with the dampening of the resulting PDF, the contribution to the peak width in the PDF, *etc*. Different refinement programs use different strategies to model the instrumental contribution. There is also typically some r-dependent broadening which is associated with both Q-dependent experimental resolution, and poor signal-to-noise in the high-Q range.

It is obvious that some of the structural and instrumental parameters are strongly correlated. The electron diffraction peak width is related to the crystal size in the sample – thus being a structural parameter. On the other hand, it is related to the focusing of the diffraction pattern and the amount of astigmatism in the projector lens. Finally, it is related to the Modulation Transfer Function of the recording medium.

The instrumental contribution to the peak width in an electron diffraction pattern is typically much larger than in an X-ray diffraction pattern. As a consequence, one expects a much stronger dampening of the PDF peak height at larger distance r. This stronger dampening of the PDF peak height imposes more severe limitations on the exact particle size determination. A similar effect is observed for the peak width in an ePDF. The increased instrumental contribution to the peak width affects the degree of confidence to which structural broadening effects such as thermal motion, and also static displacements, can be unambiguously distinguished from instrumental broadening effects.

It appears to be strongly advisable to determine the dampening contribution using a sample that has been well characterized by X-ray diffraction experiments.

11.1. Data acquisition and processing

Energy-filtered (energy slit width 10 eV) electron diffraction data of anatase was used [Fig. 6(*a*)]. The data were collected in a TITAN (FEI) transmission electron microscope operating at 300 kV (electron wavelength 0.0197 Å) collected onto a GIF 2k CCD with the primary beam shifted out of the CCD area. The data were integrated and normalized using self-written *MatLab* scripts.

Anatase has a tetragonal symmetry in space group $I4_1/amd$ and lattice parameters a = 3.785 Å, c = 9.514 Å (Hanaor & Sorrell, 2011). The structure contains Ti atoms placed at the 4*a* Wykoff position (0,0,0) and oxygen atoms at 8*e* position (0,0,*z*), with z = 0.20806 (Howard *et al.*, 1991).

11.2. Refinement in *DISCUS*

Synchrotron data obtained at the Advanced Photon Source, Argonne, USA, were used to characterize the anatase nanoparticles. Data were collected at room temperature at a wavelength of 0.5594 Å. Diffraction data were radially integrated with *FIT2D* (Hammersley *et al.*, 1996; Hammersley, 2016) and converted to the PDF with *PDFgetx3* (Juhás *et al.*, 2013). The PDF was calculated from data measured up to Q_{max} = 24.6 Å^{-1}. An elliptically shaped model of the anatase structure was refined to the experimental PDF data. Refined parameters were the lattice parameters *a* and *c*, the *z*-position of oxygen (O$_z$), a common isotropic atomic displacement parameter, a quadratic correlation term that corrects the width of PDF peaks at short distances (corrquad), an overall scale factor, and two diameters of a rotationally symmetric ellipsoid to describe the nanocrystal shape. In accordance with the tetragonal symmetry of anatase, the rotation axis was set parallel to the *c* axis. The instrumental parameters Q_{damp} and Q_{broad} were previously refined to the PDF of CeO$_2$, which had been measured under identical conditions. The shape refined to diameters of 69 Å in the *ab* plane and 95 Å along the *c* axis (Fig. 9).

These shape parameters were in turn used as fixed parameters to refine the anatase structure against the ePDF data. For this refinement instrumental parameters Q_{damp} and Q_{broad} were refined in addition to the structural parameters (*a*, *c*, O$_z$) and B_{iso}. Initial test refinement showed that the quadratic correlation parameter and Q_{broad} were highly correlated. This is not too surprising, as the large value of Q_{damp} restricts the range of the experimental PDF over which significant peaks are observed. The value of the quadratic correlation term was fixed to the value obtained from the X-ray refinement. Both refinements gave essentially identical agreement to the experimental data. The anatase lattice parameters refined to slightly different values compared with the synchrotron-based data. This reflects the uncertainty in the camera length. As expected, the instrumental parameter Q_{damp} refined to a slightly larger value of 0.0645.

11.3. Refinement in *PDFgui*

Refinements were also carried out in *PDFgui* (Farrow *et al.*, 2007). First, the synchrotron data were refined. In this case, an attenuated crystal model was used, where the PDF was simulated for a bulk crystal of the specified structure, then damped by an envelope function defined for a spherical domain. Refined parameters included lattice parameters *a* and *c*, the *z*-position of oxygen (O$_z$), isotropic atomic displacement parameters for O and Ti, and the diameter of the spherical domain. Different parameters for modifying peak widths due to short distance correlations were attempted, and the best result was found to be a constant peak sharpening factor (sratio) with a cutoff distance (rcut) of 3.8 Å, which corresponds roughly to the size of an octahedral unit in the TiO$_2$ structure. The instrumental parameters Q_{damp} and Q_{broad} were refined to the CeO$_2$ standard data set, and then kept fixed during the anatase data refinement. A model using a single atomic displacement parameter was also tested which gave a consistent value to *DISCUS*, 0.549, but with slightly poorer goodness-of-fit, approximately 3%, to the model with separate values.

The same model in *PDFgui* was refined to the ePDF data set. The reduced $F(Q)$ data set was Fourier transformed to the PDF over a range of 1.2–17.4 Å^{-1} onto a grid spacing of 0.019 Å. The same parameters for the xPDF refinement were used, except that the domain size was fixed, and Q_{damp} and Q_{broad} were refined as in the *DISCUS* refinement. As discussed above, it is well known that Q_{damp} and any domain size parameters will be highly correlated. The cutoff distance had to be increased to 4.0 Å due to the increase in both lattice parameters, which was observed consistently to the *DISCUS* refinement. Furthermore, differences in Ti versus O site ADPs could no longer be resolved (probably due to the reduced Q_{max}) and so a single value was used, which was found to be intermediate to the xPDF refined values. No significant correlations were found between the refined parameters used. Finally, two additional peaks at approximately 1.5 and 2.5 Å, which came from the unsubtracted sample support in the TEM measurement, were modelled using the first two peaks of a graphite structure phase.

11.4. Refinement in *TOPAS*

Further refinements were performed with the new PDF-functionality in *TOPAS* v6 (Coelho, 2018). The same models were used as in *PDFgui* for the xPDF and ePDF data to largely the same result. The definition used for the Q_{damp} function is formulated differently, therefore, refining to slightly different values, though to the same effect. As *TOPAS* allows new functions to be easily scripted, an attenuation envelope for a prolate spheroid was tested in addition to the spherical
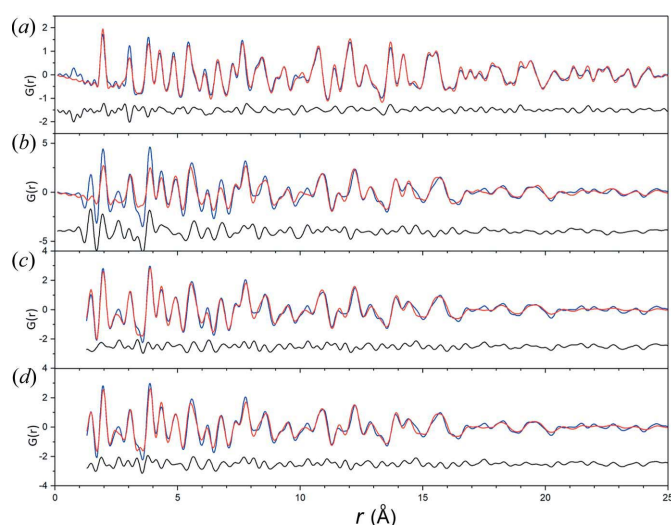

Figure 9
Results of the refinement of nanocrystalline anatase: (*a*) *DISCUS* refinement of X-ray data; (*b*) *DISCUS* refinement of ePDF; (*c*) *PDFgui* refinement of ePDF; (*d*) *TOPAS* refinement of ePDF data. The experimentally obtained data is shown in blue, the fit plots in red, the difference curves are in black.

Table 2
Values of refined parameters obtained using *DISCUS*; *PDFgui* and *TOPAS* softwares to fit the anatase structure model to the xPDF and ePDF data [ARE THE S.U.s associated with the refined values? If so, please provide.

	DISCUS		PDFgui		TOPAS	
Data	xPDF	ePDF	xPDF	ePDF	xPDF	ePDF
Q_{max} (Å⁻¹)			24.7	17.4	24.7	17.4
Range (Å)			1.3-50.0	1.3-50.0	1.3-50.0	1.3-50.0
a (Å)	3.7884	3.8480	3.7891	3.8529	3.7892	3.8499
c (Å)	9.5115	9.6580	9.5158	9.6760	9.5156	9.6774
O_z	0.2098	0.2077	0.2094	0.2089	0.2094	0.2087
Ti B_{iso}	0.545	0.539	0.392	0.676	0.396	0.520
O B_{iso}			0.899		0.958	
Diameter a-b-c (Å)	69/95	69/95 (fixed)	61	61 (fixed)	60	60 (fixed)
corrquad	0.03377	0.03377 (fixed)				
rcut (Å)			3.80	4.0	3.80	4.0
sratio			0.653	0.722	0.761	0.877
Q_{broad}	1.000×10^{-4}	5.520×10^{-3}	0.0001 (fixed)	0.0546	0.0001 (fixed)	0.0686
Q_{damp}	0.0426	0.0645	0.0373 (fixed)	0.0780	0.0886 (fixed)	0.147
scale	0.233	0.450	0.156	0.496	0.158	0.390
Rw			0.142	0.243	0.144	0.263

envelope (Lei *et al.*, 2009). The refinement resulted in an equatorial diameter of approximately 44 Å and polar diameter of 66 Å, which probably differ from *DISCUS* because the orientation does not correspond to specific directions in the crystal as would be expected. Here, it corresponds to the domain shape averaged over all crystallographic orientations, and resulted in negligible improvement over the spherical domain model. Otherwise the results, particularly for structure-specific parameters (a, c, O_z, ADPs), are highly consistent with both *PDFgui* and *DISCUS*. The trends in the resolution parameters are also consistent.

Table 2 summarizes the results of the refinement procedures. Despite slight differences in the refinement strategies, the results are essentially very similar (Fig. 9). In all three cases the refinements converged to give a reasonable figure of merit (*DISCUS* refinement did not model the contribution of
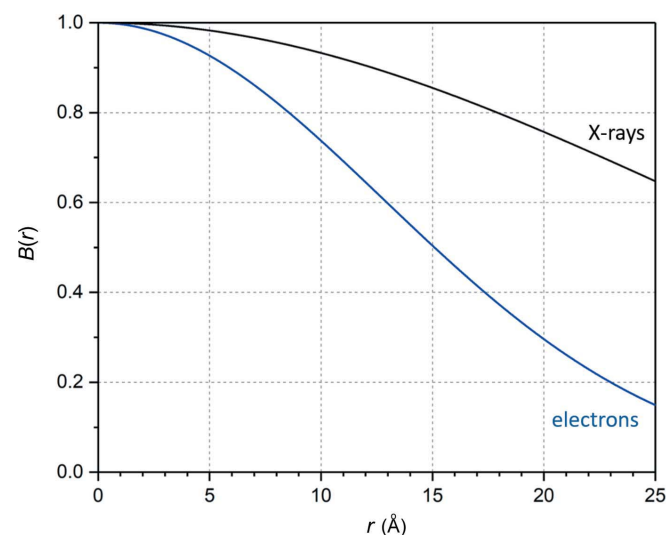

Figure 10
Envelope damping functions calculated from *PDFgui* refinement values for X-rays (black) and electrons (blue).

the carbon-supporting film, therefore, some of the low-r peaks are not fit well). All refinements were carried out using the fixed particle size (defined through the refinement of the corresponding X-ray data) with slightly different diameter and shape form. The structural parameters refined against the ePDF are two lattice parameters a and c, the z-coordinate of the oxygen atom (O_z) and ADPs.

The lattice parameters consistently refined to slightly larger values than expected, maintaining the a/c ratio. This suggests a systematic camera length error of 1.5%. This error is typical for electron diffraction and lies within the expected range. The O_z parameter refined to a reasonable value in all three cases. These results speak for suitable quality of ePDF data for structural analysis. The ADPs of the atoms refined well, yet, these are strongly correlated with other instrumental parameters, such as Q_{broad}, and the r-dependent broadening scheme used in each program.

Having fixed the particle size, we could easily extract the contribution of Q_{damp} – the Gaussian dampening envelope due to limited Q-resolution. The envelope function is calculated in the form of

$$B(r) = \exp - \frac{(rQ_{damp})^2}{2}. \tag{12}$$

Fig. 10 shows the calculated damping envelope functions $B(r)$ calculated using the values of Q_{damp} obtained in the *PDFgui* refinement of nanocrystalline anatase. As already mentioned, the instrumental peak broadening in electron diffraction data is much larger than that for X-ray sources. As a result, the effect of the damping function in direct space is much stronger. For an amorphous material with no structural peaks in the PDF after 10 Å (see Fig. 3, dashed line), the instrumental damping effect is not very significant. If a similar type of the instrumental transfer function is realized, the intensities in the PDF will be 30% damped at 10 Å, which means that in Q-space, the width of peaks is dominated by the 'crystal-size'-induced broadening. For nanocrystalline materials with extended MRO, knowledge of the instrumental damping is essential for the correct quantification of the correlation domain size.

12. Software for ePDF calculation

There are several different software packages available for the processing of electron diffraction data in order to obtain the PDF. Table 3 list these programs.

Other relevant programs include those, which calculate PDF for a known structural model: *DISCUS* (Proffen & Neder, 1999) and *PDFgui* (Juhás *et al.*, 2015).

Table 3
Available software packages for ePDF calculation from electron diffraction data.

Name	Includes diffraction data integration	Distribution
ProcessDiffraction†	Yes	Free
SUePDF (Tran *et al.*, 2017)	No	Free
eRDF Analyser (Shanmugam *et al.*, 2017)	Yes	Free
ePDF suite (NanoMegas, Belgium)	Yes	Commercial
ePDF tools (Shi *et al.*, 2019)	Yes	Free

† http://www.energia.mta.hu/~labar/ProcDif.htm

13. Conclusions and outlook

Electron PDF as a structure characterization method for disordered materials has been around for several decades now. It has been effectively applied for semi-quantitative analysis of the data: one of the striking results of ePDF being the discovery of the paracrystalline nature of amorphous silicon. The strong scattering of electrons makes ePDF an invaluable technique for structural characterization of amorphous thin films and other samples, where only a minor quantity of material exists, and as a more localized probe of structural fluctuations within the material than its bulk probe X-ray and neutron counterparts.

Experimental and mathematical methods have been developed to account for inelastic and multiple scattering which are typical problems associated with electrons. The next step towards quantitative treatment of the data is to obtain a better understanding of the instrumental contribution to the ePDF.

Direct structural properties of the model (*e.g.* lattice constants, atomic site positions) appear to refine robustly to the measured data. Other parameters such as domain shape/size, ADPs, or correlated motion terms, depending on the correction used, may correlate more strongly with instrumental parameters, making the partitioning non-trivial. The strategy in this paper, as previously presented (Abeykoon *et al.*, 2015), is a combined refinement of X-ray and electron scattering data collected from the same material, as demonstrated for anatase nanoparticles. First, the X-ray data is refined, keeping the known instrumental parameters fixed. This gives the structural characteristics of the sample. In the second step, the instrumental contribution in the ePDF is refined, keeping the previously determined structural parameters fixed. The two-step refinement shows that the effect of instrumental damping is much stronger for electrons than for X-rays. The instrument contribution for electrons has also a different character, so, possibly, special schemes should be developed to describe the Q-dependent peak broadening. It is yet unclear how different TEM settings, such as accelerating voltage, diffraction camera length, beam convergence and energy filtering, will affect the instrumental contribution, and if the instrumental contribution for a certain combination of parameters is reproducible and can be calibrated.

The history of ePDF, and the diversity of materials that ePDF has been applied to, demonstrate a large potential for the method. Therefore, we hope to witness further development and standardization of ePDF as a quantitatively reliable technique for materials characterization. This can be accomplished by addressing the most important aspects: the extraction of the single scattering component and a systematic study on instrumental contributions. Overall, we also hope to see an increase in the usage of ePDF as a complementary tool to other total scattering probes.

References

Abell, G. C. (1985). *Phys. Rev. B*, **31**, 6184–6196.
Abeykoon, A. M. M., Hu, H., Wu, L., Zhu, Y. & Billinge, S. J. L. (2015). *J. Appl. Cryst.* **48**, 244–251.
Abeykoon, M., Malliakas, C. D., Juhás, P., Božin, E. S., Kanatzidis, M. G. & Billinge, S. J. L. (2012). *Z. Kristallogr.* **227**, 248–256.
Alder, B. J. & Wainwright, T. E. J. (1957). *J. Chem. Phys.* **27**, 1208–1209.
Alder, B. J. & Wainwright, T. E. J. (1959). *J. Chem. Phys.* **31**, 459–466.
Andronis, V. & Zografi, G. (2000). *J. Non-Cryst. Solids*, **271**, 236–248.
Ankele, J. E., Mayer, J., Lamparter, P. & Steeb, S. (2005). *Z. Naturforsch.* **A60**, 459–468.
Anstis, G. R., Liu, Z. & Lake, M. (1988). *Ultramicroscopy*, **26**, 65–69.
Ashiotis, G., Deschildre, A., Nawaz, Z., Wright, J. P., Karkoulis, D., Picca, F. E. & Kieffer, J. (2015). *J. Appl. Cryst.* **48**, 510–519.
Banerjee, S., Liu, C., Lee, J. D., Kovyakh, A., Grasmik, V., Prymak, O., Koenigsmann, C., Liu, H., Wang, L., Abeykoon, A. M. M., Wong, S. S., Epple, M., Murray, C. B. & Billinge, S. J. L. (2018). *J. Phys. Chem. C*, **122**, 29498–29506.
Bassiri, R., Borisenko, K. B., Cockayne, D. J. H., Hough, J., MacLaren, I. & Rowan, S. (2011). *Appl. Phys. Lett.* **98**, 031904.
Bassiri, R., Evans, K., Borisenko, K. B., Fejer, M. M., Hough, J., MacLaren, I., Martin, I. W., Route, R. K. & Rowan, S. (2013). *Acta Mater.* **61**, 1070–1077.
Berendsen, H. J. C., Postma, J. P. M., van Gunsteren, W. F., DiNola, A. & Haak, J. R. (1984). *J. Chem. Phys.* **81**, 3684–3690.
Billinge, S. J. L. (2008). *J. Solid State Chem.* **181**, 1695–1700.
Billinge, S. J. L., DiFrancesco, R. G., Kwei, G. H., Neumeier, J. J. & Thompson, J. D. (1996). *Phys. Rev. Lett.* **77**, 715–718.
Billinge, S. J. L., McKimmy, E. J., Shatnawi, M., Kim, H., Petkov, V., Wermeille, D. & Pinnavaia, Th. J. (2005). *J. Am. Chem. Soc.* **127**, 8492–8498.
Borisenko, K. B., Chen, Y., Cockayne, D. J. H., Song, S. A. & Jeong, H. S. (2011). *Acta Mater.* **59**, 4335–4342.

electron crystallography

Borisenko, K. B., Chen, Y., Song, S. A. & Cockayne, D. J. H. (2009a). *Chem. Mater.* **21**, 5244–5251.

Borisenko, K. B., Chen, Y., Song, S. A., Nguyen-Manh, D. & Cockayne, D. J. H. (2009b). *J. Non-Cryst. Solids*, **355**, 2122–2126.

Borisenko, K. B., Haberl, B., Liu, A. C. Y., Chen, Y., Li, G., Williams, J. S., Bradby, J. E., Cockayne, D. J. H. & Treacy, M. M. J. (2012). *Acta Mater.* **60**, 359–375.

Burg, J. A., Oliver, M. S., Frot, T. J., Sherwood, M., Lee, V., Dubois, G. & Dauskardt, R. H. (2017). *Nat. Commun.* **8**, 1019.

Cerny, R. & Favre-Nicolin, V. (2007). *Z. Kristallogr.* **222**, 105–113.

Chapman, K. W., Chupas, P. J., Maxey, E. R. & Richardson, J. W. (2006). *Chem. Commun.* **38**, 4013–4015.

Chen, H. & Zuo, J.-M. (2007). *Acta Mater.* **55**, 1617–1628.

Chenoweth, K., van Duin, A. C. T. & Goddard, W. A. III (2008). *J. Phys. Chem. A*, **112**, 1040–1053.

Cockayne, D. J. H. (2007). *Annu. Rev. Mater. Res.* **37**, 159–187.

Cockayne, D. J. H. & McKenzie, D. R. (1988). *Acta Cryst.* A**44**, 870–878.

Coelho, A. A. (2018). *J. Appl. Cryst.* **51**, 210–218.

David, W. I. F. & Shankland, K. (2008). *Acta Cryst.* A**64**, 52–64.

Demirjian, B. G., Dosseh, G., Chauty, A., Ferrer, M. L., Morineau, D., Lawrence, C., Takeda, K., Kivelson, D. & Brown, S. (2001). *J. Phys. Chem. B*, **105**, 2107–2116.

Duine, P. A., Sietsma, J., Thijsse, B. J. & Pusztai, L. (1994). *Phys. Rev. B*, **50**, 13240–13249.

Egami, T. & Billinge, S. J. L. (2012). *Underneath the Bragg Peaks: Structural Analysis of Complex Materials*. Oxford: Elsevier Science.

Egerton, R. F. (1986). *Electron Energy Loss Spectroscopy in the Electron Microscope*. New York: Plenum Press.

Elliott, S. R. (1989). *Adv. Phys.* **38**, 1–88.

Eremenko, M., Krayzman, V., Gagin, A. & Levin, I. (2017). *J. Appl. Cryst.* **50**, 1561–1570.

Fantauzzi, D., Bandlow, J., Sabo, L., Mueller, J. E., van Duin, A. C. T. & Jacob, T. (2014). *Phys. Chem. Chem. Phys.* **16**, 23118–23133.

Farrow, C. L. & Billinge, S. J. L. (2009). *Acta Cryst.* A**65**, 232–239.

Farrow, C. L., Juhás, P., Liu, J. W., Bryndin, D., Božin, E. S., Bloch, J., Proffen, T. & Billinge, S. J. L. (2007). *J. Phys. Condens. Matter*, **19**, 335219.

Farrow, C. L., Ruan, C.-Y. & Billinge, S. J. L. (2010). *Phys. Rev.* B**81**, 124104.

Filik, J., Ashton, A. W., Chang, P. C. Y., Chater, P. A., Day, S. J., Drakopoulos, M., Gerring, M. W., Hart, M. L., Magdysyuk, O. V., Michalik, S., Smith, A., Tang, C. C., Terrill, N. J., Wharmby, M. T. & Wilhelm, H. (2017). *J. Appl. Cryst.* **50**, 959–966.

Gilbert, B., Erbs, J. J., Penn, R. L., Petkov, V., Spagnoli, D. & Waychunas, G. A. (2013). *Am. Mineral.* **98**, 1465–1476.

Gilbert, B., Huang, F., Zhang, H., Waychunas, G. A. & Banfield, J. F. (2004). *Science*, **305**, 651–654.

Gorelik, T. E., Schmidt, M. U., Kolb, U. & Billinge, S. J. L. (2015). *Microsc. Microanal.* **21**, 459–471.

Gujral, A., Yu, L. & Ediger, M. D. (2018). *Curr. Opin. Solid State Mater. Sci.* **22**, 49–57.

Hadermann, J. & Palatinus, L. (2019). *Acta Cryst.* B**75**, 462.

Hall, L. E. & Cockayne, D. J. H. (1993). *Micron*, **24**, 357–362.

Hammersley, A. P. (2016). *J. Appl. Cryst.*, **49**, 646–652.

Hammersley, A. P., Svensson, S. O., Hanfland, M., Fitch, A. N. & Häusermann, D. (1996). *High. Pressure Res.* **14**, 235–248..

Hanaor, D. A. H. & Sorrell, C. C. (2011). *J. Mater. Sci.* **46**, 855–874.

Hancock, B. C., Shalaev, E. Y. & Shamblin, S. L. (2002). *J. Pharm. Pharmacol.* **54**, 1151–1152.

Hart, M. J., Bassiri, R., Borisenko, K. B., Véron, M., Rauch, E. F., Martin, I. W., Rowan, S., Fejer, M. M. & MacLaren, I. (2016). *J. Non-Cryst. Solids*, **438**, 10–17.

Hirata, A., Guan, P., Fujita, T., Hirotsu, Y., Inoue, A., Yavari, A. R., Sakurai, T. & Chen, M. (2011). *Nat. Mater.* **10**, 28–33.

Hirata, A., Hirotsu, Y., Ohkubo, T., Hanada, T. & Bengus, V. Z. (2006a). *Phys. Rev. B*, **74**, 214206-1-9.

Hirata, A., Hirotsu, Y., Ohkubo, T., Tanaka, N. & Nieh, T. G. (2006b). *Intermetallics*, **14**, 903–907.

Hirata, A., Kang, L. J., Fujita, T., Klumov, B., Matsue, K., Kotani, M., Yavari, A. R. & Chen, M. W. (2013). *Science*, **341**, 376–379.

Hirata, A., Morino, T., Hirotsu, Y., Itoh, K. & Fukunaga, T. (2007). *Mater. Trans.* **48**, 1299–1303.

Hirotsu, Y., Ohkubo, T., Bae, I. T. & Ishimaru, M. (2003). *Mater. Chem. Phys.* **81**, 360–363.

Howard, C. J., Sabine, T. M. & Dickson, F. (1991). *Acta Cryst.* B**47**, 462–468.

Hristova-Vasileva, T., Petrik, P., Nesheva, D., Fogarassy, Z., Lábár, J., Kaschieva, S., Dmitriev, S. N. & Antonova, K. (2018). *J. Appl. Phys.* **123**, 195303.

Huang, P. Y., Kurasch, S., Alden, J. S., Shekhawat, A., Alemi, A. A., McEuen, P. L., Sethna, J. P., Kaiser, U. & Muller, D. A. (2013). *Science*, **342**, 224–227.

Huang, P. Y., Kurasch, S., Srivastava, A., Skakalova, V., Kotakoski, J., Krasheninnikov, A. V., Hovden, R., Mao, Q., Meyer, J. C., Smet, J., Muller, D. A. & Kaiser, U. (2012). *Nano Lett.* **12**, 1081–1086.

Ishimaru, M. (2006). *Nucl. Instrum. Methods Phys. Res. B*, **250**, 309–314.

Jensen, K. M., Christensen, M., Juhas, P., Tyrsted, C., Bøjesen, E. D., Lock, N., Billinge, S. J. L. & Iversen, B. B. (2012). *J. Am. Chem. Soc.* **134**, 6785–6792.

Juhás, P., Davis, T., Farrow, C. L. & Billinge, S. J. L. (2013). *J. Appl. Cryst.* **46**, 560–566.

Juhás, P., Farrow, C., Yang, X., Knox, K. & Billinge, S. (2015). *Acta Cryst.* A**71**, 562–568.

Keen, D. A. (2001). *J. Appl. Cryst.* **34**, 172–177.

Kirk, D., Kohn, A., Borisenko, K. B., Lang, C., Schmalhorst, J., Reiss, G. & Cockayne, D. J. H. (2009). *Phys. Rev. B*, **79**, 014203.

Kis, V. K., Posfai, M. & Labar, J. L. (2006). *Atmos. Environ.* **40**, 5533–5542.

Klement, W. Jr, Willens, R. H. & Duwez, P. (1960). *Nature*, **187**, 869–870.

Kovács Kis, V., Dódony, I. & Lábár, J. L. (2006). *Eur. J. Mineral.* **18**, 745–752.

Kuhs, W. F. & Lehmann, M. S. (1983). *J. Phys. Chem.* **87**, 4312–4313.

Lábár, J. L., Adamik, M., Barna, B. P., Czigány, Zs., Fogarassy, Zs., Horváth, Z. E., Geszti, O., Misják, F., Morgiel, J., Radnóczi, G., SáFrán, G., Székely, L. & Szüts, T. (2012). *Microsc. Microanal.* **18**, 406–420.

Lábár, J. L. & Das, P. P. (2017). *Microsc. Microanal.* **23**, 647–660.

Lei, M., de Graff, A. M. R., Thorpe, M. F., Wells, S. A. & Sartbaeva, A. (2009). *Phys. Rev. B*, **80**, 024118.

Li, G., Borisenko, K. B., Chen, Y., Nguyenmanh, D., Ma, E. & Cockayne, D. J. H. (2009). *Acta Mater.* **57**, 804–811.

Li, Z., Mu, X., Zhao-Karger, Z., Diemant, T., Behm, R. J., Kübel, C. & Fichtner, M. (2008). *Nat. Commun.* **9**, 5115.

Machon, D., Meersman, F., Wilding, M. C., Wilson, M. & McMillan, P. F. (2014). *Prog. Mater. Sci.* **61**, 216–282.

Manceau, A., Skanthakumar, S. & Soderholm, L. (2014). *Am. Mineral.* **99**, 102–108.

McCulloch, D. G., McKenzie, D. R., Goringe, C. M., Cockayne, D. J. H., McBride, W. & Green, D. C. (1999). *Acta Cryst.* A**55**, 178–187.

McGreevy, R. L. & Pusztai, L. (1988). *Mol. Simul.* **1**, 359–367.

Michel, F. M., Ehm, L., Antao, S. M., Lee, P. L., Chupas, P. J., Liu, G., Strongin, D. R., Schoonen, M. A. A., Phillips, B. L. & Parise, J. B. (2007). *Science*, **316**, 1726–1729.

Mishima, O. (2010). *Proc. Jpn. Acad. Ser. B*, **86**, 165–175.

Mitchell, D. R. G. (2008). *Microsc. Res. Tech.*, **71**, 588–593.

Mu, X. (2013). Dissertation, TU Darmstadt, Germany (pp. 91–95).

Mu, X., Neelamraju, S., Sigle, W., Koch, C. T., Totò, N., Schön, J. C., Bach, A., Fischer, D., Jansen, M. & van Aken, P. A. (2013). *J. Appl. Cryst.* **46**, 1105–1116.

Mu, X., Sigle, W., Bach, A., Fischer, D., Jansen, M. & van Aken, P. A. (2014). *Z. Anorg. Allg. Chem.* **640**, 1868–1875.

Murawski, C., Elschner, C., Lenk, S., Reineke, S. & Gather, M. C. (2018). *Org. Electron.* **53**, 198–204.

Nakamura, N., Terban, M. W., Billinge, S. J. L. & Reeja-Jayan, B. (2017). *J. Mater. Chem. A*, **5**, 18434–18441.

Ou, J. J. & Chen, S. H. (1998). *J. Comput. Chem.* **19**, 86–93.

Page, K., Proffen, Th., Terrones, H., Terrones, M., Lee, L., Yang, Y., Stemmer, S., Seshadri, R. & Cheetham, A. K. (2004). *Chem. Phys. Lett.* **393**, 385–388.

Pagon, A. M., Partridge, J. G., Hubbard, P., Taylor, M. B., McCulloch, D. G., Doyle, E. D., Latham, K., Bradby, J. E., Borisenko, K. B. & Li, G. (2010). *Surf. Coat. Technol.* **204**, 3552–3558.

Pauly, T. R., Liu, Y., Pinnavaia, T. J., Billinge, S. J. L. & Rieker, T. P. (1999). *J. Am. Chem. Soc.* **121**, 8835–8842.

Petersen, T. C., McBride, W., McCulloch, D. G., Snook, I. K. & Yarovsky, I. (2005). *Ultramicroscopy*, **103**, 275–283.

Petkov, V., Billinge, S. J. L., Heising, J. & Kanatzidis, M. G. (2000). *J. Am. Chem. Soc.* **122**, 11571–11576.

Petkov, V., Difrancesco, R. G., Billinge, S. J. L., Acharya, M. & Foley, H. C. (1999). *Philos. Mag. B*, **79**, 1519–1530.

Pradhan, S. K., Mao, Y., Wong, S. S., Chupas, P. & Petkov, V. (2007). *Chem. Mater.* **19**, 6180–6186.

Prill, D., Juhás, P., Schmidt, M. U. & Billinge, S. J. L. (2015). *J. Appl. Cryst.* **48**, 171–178.

Prince, E. (2004). Editor. *International Tables for Crystallography*, Vol. C. Dordrecht/Boston/London: Kluwer Academic Publishers.

Proffen, Th. & Neder, R. B. (1999). *J. Appl. Cryst.* **32**, 838–839.

Rams-Baron, M., Jachowicz, R., Boldyreva, E., Zhou, D., Jamroz, W. & Paluch, M. (2018). *Amorphous Drugs: Benefits and Challenges*. Springer.

Reimer, L. & Kohl, H. (2008). *Transmission Electron Microscopy*: *Physics of Image Formation*. Springer Series in Optical Sciences.

Rez, D., Rez, P. & Grant, I. (1994). *Acta Cryst.* **AS0**, 481–497.

Ruan, C.-Y., Murooka, Y., Raman, R. K., Murdick, R. A., Worhatch, R. J. & Pell, A. (2009). *Microsc. Microanal.* **15**, 323–337.

Shanmugam, J., Borisenko, K. B., Chou, Y.-J. & Kirkland, A. I. (2017). *SoftwareX*, **6**, 185–192.

Sheng, H. W., Liu, H. Z., Cheng, Y. Q., Wen, J., Lee, P. L., Luo, W. K., Shastri, S. D. & Ma, E. (2007). *Nat. Mater.* **6**, 192–197.

Shi, H., Luo, M. & Wang, W. (2019). *Comput. Phys. Commun.* **238**, 295–301.

Shmueli, U. (2007). *Theories and Techniques of Crystal Structure Determination*. Oxford University Press.

Sproul, A., McKenzie, D. R. & Cockayne, D. J. H. (1986). *Philos. Mag. B*, **54**, 113–131.

Stachurski, Z. H. (2013). *Phys. Procedia*, **48**, 55–58.

Stuckelberger, M., Biron, R., Wyrsch, N., Haug, F.-J. & Ballif, C. (2017). *Renewable Sustainable Energ. Rev.* **76**, 1497–1523.

Tran, D. T., Svensson, G. & Tai, C.-W. (2017). *J. Appl. Cryst.* **50**, 304–312.

Transue, W. J., Nava, M., Terban, M. W., Yang, J., Greenberg, M. W., Wu, G., Foreman, E. S., Mustoe, C. L., Kennepohl, P., Owen, J. S., Billinge, S. J. L., Kulik, H. J. & Cummins, C. C. (2019). *J. Am. Chem. Soc.* **141**, 431–440.

Treacy, M. M. J. & Borisenko, K. B. (2012). *Science*, **335**, 950–953.

Treacy, M. M. J., Gibson, J. M., Fan, L., Paterson, D. J. & McNulty, I. (2005). *Rep. Prog. Phys.* **68**, 2899–2944.

Van Duin, A. C. T., Dasgupta, S., Lorant, F. & Goddard, W. A. III (2001). *J. Phys. Chem.* **A105**, 1089–5639.

Willinger, E., Massué, C., Schlögl, R. & Willinger, M. G. (2017). *J. Am. Chem. Soc.* **139**, 12093–12101.

Wu, Z. W., Li, M. Z., Wang, W. H. & Liu, K. X. (2015). *Nat. Commun.* **6**, 6035.

Yan, A., Sun, T., Borisenko, K. B., Buchholz, D. B., Chang, R. P. H., Kirkland, A. I. & Dravid, V. P. (2012). *J. Appl. Phys.* **112**, 054907.

Yue, X., Inoue, A., Liu, C.-T. & Fan, C. (2017). *Mater. Res.* **20**, 326–338.

Zachariasen, W. H. (1932). *J. Am. Chem. Soc.* **54**, 3841–3851.

Zeng, Q., Sheng, H., Ding, Y., Wang, L., Yang, W., Jiang, J.-Z., Mao, W. L. & Mao, H.-K. (2011). *Science*, **332**, 1404–1406.

Zewail, A. H. (2006). *Annu. Rev. Phys. Chem.* **57**, 65–103.

Zhu, C., Mu, X., Popovic, J., Weichert, K., van Aken, P. A., Yu, Y. & Maier, J. (2014). *Nano Lett.* **14**, 5342–5349.